Time-resolved studies of ultrafast wavepacket dynamics in hydrogen molecules

Calvert, C., Bryan, W. A., Newell, A., & Williams, I. (2010). Time-resolved studies of ultrafast wavepacket dynamics in hydrogen molecules. Physics Reports, 491(1), 1-28. DOI: 10.1016/j.physrep.2009.12.004

Published in:
Physics Reports

Physics Reports 491 (2010) 1–28

Contents lists available at ScienceDirect

Physics Reports

journal homepage: www.elsevier.com/locate/physrep

Time-resolved studies of ultrafast wavepacket dynamics in hydrogen molecules

C.R. Calvert [a,*], W.A. Bryan [b,d], W.R. Newell [c], I.D. Williams [a]

[a] Department of Physics and Astronomy, Queen's University Belfast, BT7 1NN, UK
[b] Department of Physics, Swansea University, Swansea, SA2 8PP, UK
[c] Department of Physics and Astronomy, University College London, WC1E 6BT, UK
[d] Central Laser Facility, STFC Rutherford Appleton Laboratory, Didcot, OX11 0QX, UK

ARTICLE INFO

Article history:
Accepted 1 December 2009
Available online 4 December 2009
editor: J. Eichler

Keywords:
Ultrafast
Pump-probe
Wavepacket revival
Femtosecond
Time-resolved
Hydrogen
Deuterium

ABSTRACT

Recent advances in the study of quantum vibrations and rotations in the fundamental hydrogen molecules are reported. Using the deuterium molecules (D_2^+ and D_2) as exemplars, the application of ultrafast femtosecond pump-probe experiments to study the creation and time-resolved imaging of coherent nuclear wavepackets is discussed. The ability to study the motion of these fundamental molecules in the time-domain is a notable milestone, made possible through the advent of ultrashort intense laser pulses with durations on sub-vibrational (and sub-rotational) timescales. Quantum wavepacket revivals are characterised for both vibrational and rotational degrees of freedom and quantum models are used to provide a detailed discussion of the underlying ultrafast physical dynamics for the specialist and non-specialist alike.

Contents

* Corresponding author. Tel.: +44 2890973699.
E-mail addresses: c.calvert@qub.ac.uk (C.R. Calvert), i.williams@qub.ac.uk (I.D. Williams).

0370-1573/$ – see front matter © 2009 Elsevier B.V. All rights reserved.
doi:10.1016/j.physrep.2009.12.004

1. Introduction

Innovative developments in research light sources invariably lead to advances in our understanding of atomic and molecular behaviour. The advent of the synchrotron light source, for example, paved the way for the detailed study of two electron excitation in helium [1], whilst the arrival of tuneable lasers enabled narrow-bandwidth radiation to precisely probe resonant transitions between vibrational, rotational and electronic energy levels in fundamental molecules [2]. Spectroscopic studies of this kind rely on very narrow bandwidths to achieve the high resolution necessary to distinguish closely-lying energy states. However the uncertainty principle dictates that precision in energy can only be achieved by sacrificing precision in time, such that highly accurate spectroscopic techniques are not generally suitable for highly resolved measurements of ultrafast processes in the time domain. In order to study time evolving processes with lasers, it is desirable to use pulsed laser sources of durations comparable to, or shorter than, the natural timescale of interest.

The development of short pulse lasers towards this goal has required the use of sources that can generate a large bandwidth of radiation (hence containing a range of photon energies), and techniques have been established to enable pulses to be produced on femtosecond (fs) timescales, where 1 fs $= 10^{-15}$ s. This has been made possible through the use of Ti:Sapphire lasers [3] (conventionally centred at a wavelength of $\lambda = 800$ nm) and the application of chirped-pulse-amplification [4], enabling the production of intense femtosecond pulses which may be used as tools in many areas of scientific research.

With the initial development of such short pulse lasers, Zewail and others began to study molecular reactions in the time domain, opening a new field of 'femtochemistry' [5,6], using IR pulses with durations of 50–100 fs. More recently it has become possible to produce pulses of the order of 10 fs, where there are only a few-cycles of the carrier field in the pulse envelope (for 800 nm, 1 cycle $= 8/3$ fs). Such pulses will typically have bandwidths of around 100 nm and pulse energies of less than 1 mJ. However the squeezing of the pulse energy into the ultrashort time period, combined with spatial squeezing by focussing to a small spot size, leads to very high instantaneous intensities. Indeed the electric field strength generated by the radiation can be comparable to, or greater than, the binding energy of an electron. In this strong field regime an H_2 molecule can be ionised by an electron tunnelling through the field-distorted potential well and, in a similar manner, dissociation or further ionisation of the H_2^+ molecular ion can also be induced by the laser field. These ionisation and fragmentation processes have been studied in great detail in recent years as the hydrogen diatomics are prototypal molecules in which to study such fundamental dynamics (see review articles [7–9] and references therein).

In the past 4–5 years, an extensive effort has also been expended on *time-resolved* pump-probe studies of hydrogen molecules. This has been a research topic attracting interest from a number of international groups, including prominent research teams from the Max-Planck-Institut für Kernphysik (Heidelberg) [10], the NRC Steacie Institute for Molecular Sciences (Ottawa) [11], the James R. Macdonald Laboratory at Kansas State University [12], the Blackett Laboratory at Imperial College London [13] and a collaboration between FOM-AMOLF (Amsterdam) and the Max-Planck-Institute für Quantenoptik (Garching) [14], as well as work carried out by the authors [15].

In recent pump-probe experiments, the aim has been to use intense laser pulses of the order of 10 fs duration to induce and characterise the temporal evolution of rotational and vibrational dynamics in these most fundamental diatomics. The ability to manipulate and observe these molecules in this way represents a significant milestone in time-resolved studies of molecular motion, providing insight into some of the fastest and most fundamental molecular behaviour. The deuterium isotope, D_2, is generally used in preference to H_2 due to its larger reduced mass, which enforces a slightly longer timescale on the characteristic dynamics. As D_2^+ retains the fundamental nature of the three particle problem, it is equally tractable to theoretical approaches and is therefore an ideal test-bed for time-resolved studies of the hydrogen molecule.

In this report, emphasis is placed on describing the key dynamics that have been elucidated in recent ultrafast pump-probe experiments on D_2 and care has been taken to provide a detailed discussion that is accessible to both the specialist and non-specialist alike. The reader will be given an in-depth insight into the dynamics that have been unveiled, described with the help of theoretical models and sample experimental results obtained by the authors. In this way, the characterisation of the time-evolving ultrafast vibrations and rotations will be described, with the significant contributions in this area of research (from many international groups) discussed and itemised in the extensive list of references.

2. Experimental approach

An experimental arrangement for studying intense short pulse interactions with molecular targets in the gas phase requires two main components — a laser system and an interaction/analysis arrangement. In order to generate short pulse durations, Ti:Sapphire laser systems[1] utilising chirped-pulse-amplification schemes are commonly used and can be coupled with some secondary compression technique in order to obtain pulse durations of the order of 10 fs or shorter.

A typical interaction chamber for studying molecular fragmentation in femtosecond pulses will contain a diffuse gas phase target maintained under ultrahigh vacuum conditions (pressure $<10^{-9}$ mBar). Detection and analysis of interaction products can be carried out using a time-of-flight mass spectrometer (TOFMS) (e.g [16]), from which energetics of charged

[1] So-called because the lasing medium is a sapphire crystal (Al_2O_3) doped with titanium ions. Ti:Sapphire lasers emit near infra-red light with a broad bandwidth, enabling the production of short, femtosecond pulses.

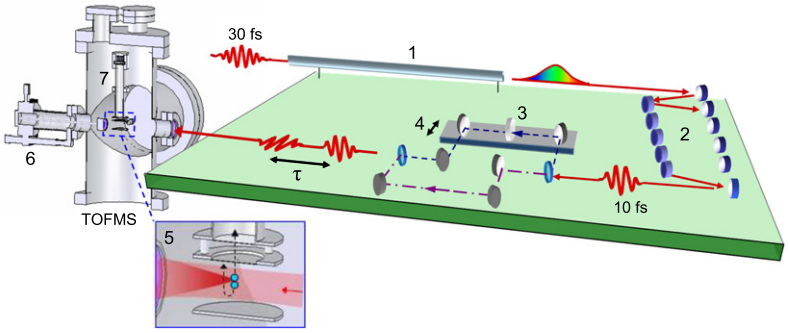

Fig. 1. Schematic of a typical experimental arrangement for pump-probe studies of gas phase molecular targets, with typical parameters quoted from the laser system in [18]. Linearly polarised pulses (30 fs) from a Ti:Sapphire system are aligned into a hollow-fibre waveguide capillary (1) and spectrally broadened (from $\Delta\lambda \approx 40$ nm to >100 nm) by self phase modulation. Temporal compression, enforced by a set of multilayered chirped mirrors (2), produces 10 fs pulses which proceed to a Mach–Zehnder interferometer. The beam can be split into two co-propagating components, the fixed path (purple — · — line) and the variable path (blue — — — line), which are recombined collinearly at a final beam-splitter. A translation stage (4) that can be moved in increments of 0.05 μm will provide a variable temporal delay, τ (in steps of 1/3 fs) between the emerging pulses. A half wave plate (3) can be used in either path to rotate the polarisation axis (initially vertical) of the beam. The resulting pulses can be aligned into a Time of Flight Mass Spectrometer (as shown by a cut-away here) and reflection focussed (5) onto the gas target. The position of the focussing mirror can typically be adjusted by an XYZ manipulator (6). The resulting charged products from the interaction are extracted by a weak homogeneous electric field, through a drift tube and collected at a micro channel plate detector (7). With flight times recorded on an digital storage oscilloscope, the energetics of the fragmentation processes can be deduced.

fragments may be extracted, or via either the COLTRIMS[2] [17] or velocity-map imaging [131] techniques, where particles arriving from the same fragmentation event can be measured in coincidence and from which particle momenta may be deduced. These techniques have all been extensively used to analyse the fragmentation events from strong-field interactions with gas targets. In this section a typical TOFMS arrangement for studies of short pulse interactions with a gas-phase target will be outlined.[3] Such an experimental arrangement is displayed schematically in Fig. 1.

The starting point for the laser system is to have short pulses at relatively high intensities, with as high a repetition rate as possible. Ti:Sapphire systems that are commercially available can typically provide pulses of 25–35 fs at energies of 1–10 mJ and at kHz repetition rates. In order to study dynamics in hydrogen molecules on a sub-vibrational timescale, these pulses must be further compressed in time. This can be done, as depicted in Fig. 1, by aligning the beam into a hollow fibre waveguide capillary containing an inert gas, differentially pumped along the length of the hollow fibre. This capillary serves to spectrally broaden the laser light through self phase modulation [19] and this can achieve a bandwidth upwards of 100 nm. A set of multilayered, chirped mirrors [20] can then be used to temporally compress these broadened pulses to an on-target duration of 10 fs or less, with appropriate compensation made for dispersion at subsequent optical surfaces. Temporal and spectral pulse characterisation can be performed by Frequency Resolved Optical Gating (FROG) [21] or via Spectral Phase Interferometry for Direct Electric-field Reconstruction (SPIDER) [22].

The resulting few-cycle IR pulses can then be prepared for pump-probe studies. This is typically done via either a Mach–Zehnder (MZ) interferometer (e.g. [23,24]) or through the innovative 'core-annulus technique' (e.g. [25,26]). These two alternative methods will now be discussed in brief.

An MZ interferometer is depicted in Fig. 1 and enables the beam to be split into two separate components of comparable energy and then recombined collinearly. The use of a translation stage in the interferometer enables the path length, and thus propagation time, of the pulses to be altered with high precision. This provides a finely adjustable pump-probe delay time, τ. The orientation of the linear polarisation vector of the pulses may also be manipulated by use of a half wave plate, which can be placed in either path of the interferometer. It is important to note that most beam splitters used in this type of interferometer arrangement will exhibit polarisation dependence for both energy transmission and temporal dispersion of the pulses. Thus for different polarisation configurations, pulse diagnostics must be carefully monitored. In the MZ interferometer, a significant portion of energy is unavoidably lost at the recombining beam splitters but the collinear propagation makes it possible for the spatial and temporal overlap of the pump and probe pulses to be perfectly obtained.

The alternative 'core-annulus technique' operates in a different manner and does not result in energy loss at recombining beam splitters. The technique is explained in [26], where the beam is split spatially as it passes through a glass window which has a core circle cut from the centre. The inner part of the beam subsequently passes through a small window of the same thickness, the same size as the core which was removed from the larger window. When these windows are both perfectly perpendicular to the direction of propagation, a single pulse is transmitted. If the outer annulus is rotated slightly, the thickness of glass that the outer pulse portion propagates through is increased and the pulse is delayed with respect to the inner core. This technique has its advantages, as the pump and probe beams will naturally co-propagate. However

2 COLd Target Recoil Ion Momentum Spectroscopy.

3 For more details on the complementary COLTRIMS technique, the interested reader is referred to [17].

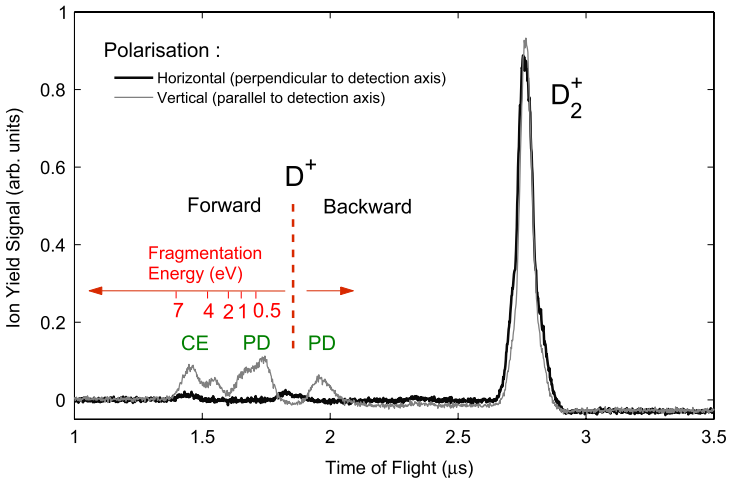

Fig. 2. Typical time-of-flight spectra for single pulse interactions with a D_2 gas target. Black line — 13 fs pulse (6×10^{14} W cm^{-2}) with polarisation perpendicular to spectrometer detection axis. Grey line — 12 fs pulse (6×10^{14} W cm^{-2}), polarisation parallel to detection axis. Both spectra exhibit a D_2^+ yield from ionisation of D_2. The deuterons (D^+) from fragmentation events are extracted along the detection axis direction, with those arriving around 1.8 μs having minimal fragmentation energy. Products initially projected towards the detector ('forward') arrive before the red dashed line, with highest energy products arriving first. The 'backward' projected products are turned around by the extraction field and arrive later, with some high energy products lost due to the acceptance angle of the spectrometer. The D^+ signal arises from Coulomb Explosion (CE) or Photodissociation (PD) processes, see text for details.

at long delay times there will be problems due to significant cropping/diffraction of the beam such that the quality of the spatial overlap will be inevitably compromised. There will also be temporal dispersion due to transmission through the glass, leading to variation in key pulse parameters such as pulse duration and energy.

Although both techniques have significant merits, the MZ technique is more reliable for accurate studies over long delay ranges, with better temporal consistency of the spatial overlap as a function of time delay [27] and the parameters of the pump and probe pulses will not change across the range of τ values. Furthermore, in the core-annulus technique the pump and probe must have the same polarisation whereas the MZ technique allows polarisation control, a feature which will be seen to be important for the studies reported in this article.

The resulting MZ interferometer pulses can then be aligned into the TOFMS interaction chamber and reflection focussed onto a gas target. For such short pulses it is crucial that temporal dispersion/chirping effects of the pulse are minimised in the path of the beam, thus necessitating the use of a mirrored focussing technique rather than a conventional focussing lens.

Subsequent ionisation/fragmentation products from the laser interaction with the gas target can then be extracted by a uniform weak electric field through an aperture in the TOFMS. The aperture serves to limit the ion sampling to the highest intensity point of the laser focus and restrict the angular acceptance of the system to fragments projected parallel to the detection axis, i.e. vertical in Fig. 1.

For example, a deuteron with 1 eV energy will experience an acceptance angle of less than 4 degrees for the geometry utilised in [27]. This is extremely important in these studies due to the angular dependence of the fragmentation mechanisms. This will be explained in detail in Section 3. After extraction, the products pass through an acceleration region and a field free drift tube prior to collection at a microchannel plate (MCP) detector, with the corresponding TOF being recorded. It is possible to adjust the position of the internal spherical mirror (and thus the laser focus) if it is mounted on a three axis 'XYZ' micrometer, adjustable from outside the vacuum chamber. The beam alignment and mirror position should be carefully manipulated in order to optimise the ion signal strength. The operation of the TOFMS in Wiley–McLaren mode [16] serves to enable fragment energies to be readily calculated from the recorded ion flight times.

Prior to considering pump-probe studies of the D_2 target, it is crucial to understand the effects of single pulse interactions with the molecule. This will be described presently using a typical diagnostic, where time-of-flight spectra for the separate interferometer pulses are recorded. This can be done by blocking the appropriate path in the interferometer, permitting only the desired pulse to interact with the D_2 target. Time-of-flight spectra are displayed in Fig. 2 for both vertical and horizontal polarisation orientations, i.e. parallel and perpendicular to the detection axis respectively.

3. Intense-field femtosecond fragmentation and ionisation of D_2

The intense-field ionisation and dissociation processes of D_2 and D_2^+ and their isotopic variants (H_2 and H_2^+, HD and HD^+) in femtosecond IR pulses have attracted much interest in recent years. The mechanisms have been described in detail in recent review articles [7–9] and studies of the fragmentation dynamics and energetics continue to yield interesting developments for both gas phase neutral targets (e.g. [28–31] and ion beam targets [32–39].

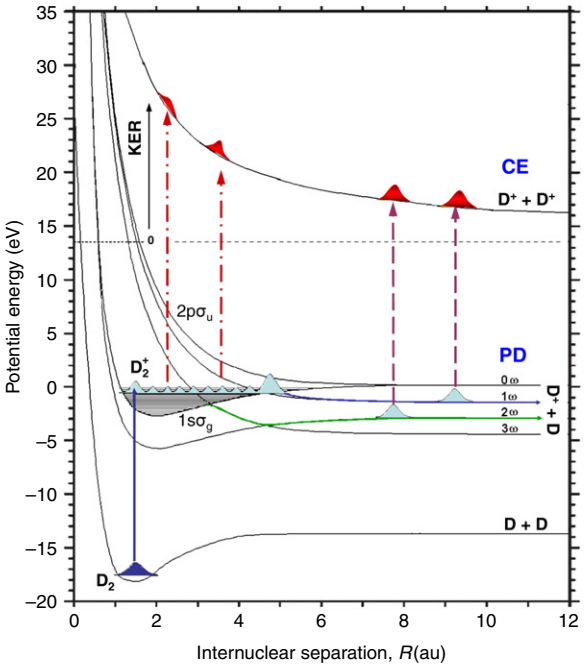

Fig. 3. Schematic of intense field pulse interactions with a D_2 target. The pulse may tunnel ionise D_2 to create a coherent wavepacket on the $1s\sigma_g$ surface of D_2^+. This wavepacket may further undergo photodissociation (PD) by net absorption of one (1ω) or two (2ω) photons, proceeding to large R to give $D^+ + D$ products. Alternatively, denoted by the red ($-\cdot-$) and purple ($---$) lines respectively, the bound or dissociating wavepacket may be projected onto the Coulomb potential to give a ($D^+ + D^+$), with the kinetic energy release (KER) dictated by the R value at which the ionisation occurs. This channel is denoted as Coulomb explosion (CE). Depending on pulse duration and intensity, the secondary fragmentation steps (PD and CE) may occur either within the ionising pulse (discussed in Section 3) or by the application of a secondary pulse to probe the D_2^+ system (to be discussed from Section 4 onwards).

The majority of the formative studies of these molecules have utilised pulses of the order of 30–50 fs, but with shorter pulse durations now available, comparisons have recently been made between the effects of 'long' (25 fs) and 'short' (7 fs) pulses (e.g. [40,41]).

In many studies to date, the energetics of molecular breakup have been analysed in precise detail and many subtle effects in dissociative pathways have been elucidated. The full extent of these investigations will not be discussed in detail here, as an exhaustive discussion would easily comprise a full review article in itself. As such, for any information beyond the scope of what is explained here, the interested reader is encouraged to read the aforementioned articles and references therein.

What is of primary importance to this report is a basic understanding of the underlying fragmentation mechanisms. This will provide a platform from which the initiation and imaging of the wavepacket dynamics, to be discussed later in the report, can be understood. With this in mind, the fragmentation yields from single pulse interactions will be briefly explained using typical experimental results (Fig. 2) and the associated potential surfaces of the deuterium molecule (Fig. 3).

The time-of-flight spectra in Fig. 2 were taken using single pulses from an experimental configuration similar to that in Fig. 1. It can be seen that large yields of D_2^+ ions are formed and extracted along the detection axis for both of the pulse polarisation orientations. At the pulse intensities of interest here, this initial ionisation of the D_2 target may be explained in terms of quantum mechanical tunnelling. This process is highly non-linear with intensity and is best understood as a field-induced ionisation process, where the laser pulse is considered in terms of the oscillating electric field. The electric field of the pulse interacts with the target to perturb the barrier which binds the electron to the molecule and, at high enough intensities, this barrier may be sufficiently lowered to enable tunnel ionisation to occur resulting in the escape of one electron. It is convenient to discuss the remaining molecular system within the Born–Oppenheimer approximation, such that this tunnel ionisation launches a coherent wavepacket on the ground electronic surface of the D_2^+ ion.

In D_2^+ (and H_2^+/HD^+) there are two energetically low-lying electronic states that are key to the intense-field interaction dynamics pertinent to this article. The ground electronic state is commonly denoted as $1s\sigma_g$ (g $\Rightarrow$ gerade, symmetric) and the lowest lying excited state is referred to as $2p\sigma_u$ (ungerade, antisymmetric).

The electronic wavefunctions, and the associated quantised energies of these states, vary as a function of the internuclear separation R. For each R value, the corresponding electronic wavefunction for the $2p\sigma_u$ state will infer an equal probability of the electron being localised on one of the two nuclei whereas in the $1s\sigma_g$ state, the electron is more likely to be found *between* the two nuclei. Correspondingly, the $1s\sigma_g$ is a bound state and $2p\sigma_u$ is dissociative, this is reflected in the associated potential surfaces depicted in Fig. 3.

Any bound ions created from the tunneling ionisation $D_2 \rightarrow D_2^+$ will be nascent on the $1s\sigma_g$ surface in a broad vibrational distribution, this is addressed in detail in Section 5. After the electron is ejected, the resulting bound D_2^+ ions that survive the

subsequent evolution of the laser pulse can be extracted and collected at an MCP detector. By momentum conservation, the D_2^+ ion does not gain a large fragmentation velocity (it is much heavier than the electron) and is thus extracted via the small aperture regardless of any directed projection due to the pulse polarisation. Furthermore the D_2 target can be assumed to be initially isotropically distributed, so any angular/orientation dependence of the ionisation rate will not be a factor in this experimental technique.

At earlier flight times however, there are noticeable differences between the two spectra. The peaks arriving in the region of 1.4 to 2.1 μs are due to D^+ ions arising from fragmentation of the molecule. The difference between the two spectra is now due to an orientation dependence of the fragmentation mechanisms. Firstly, consider the case of vertical polarisation (parallel to detection axis). The D^+ signal arises from two main processes, photodissociation (PD) or Coulomb explosion (CE) of the molecule. Energetically, PD occurs in the range 0–1.5 eV and CE between 3 and 7 eV. These mechanisms will now be respectively described in detail.

Photodissociation occurs as a secondary step to the initial tunnel ionisation, where: $D_2 \rightarrow D_2^+ \rightarrow D^+ + D$. Here the coherent wavepacket that is initiated in D_2^+ begins to move on the $1s\sigma_g$ surface (the bond expands to a larger R value) and subsequently undergoes further net-absorption of one[4] or more photons. For the pulse intensities considered here, PD will proceed mainly via net 1ω or 2ω processes, although it is worth noting that higher order processes have been observed elsewhere [34,35], under different conditions.

This process is displayed in Fig. 3 in terms of the D_2^+ potential curves shifted by multiples of photon energy. The $1s\sigma_g$ potential is the ground electronic state of the D_2^+ ion and $2p\sigma_u$ is the lowest lying excited state. Energetically, this dissociative state tends towards $1s\sigma_g$ (as $R \rightarrow \infty$) and, at the intensities considered here, interactions between these two low lying electronic states need only be considered, i.e. coupling to other excited states in the D_2^+ system is negligible.

Consider the centre wavelength of 800 nm, corresponding to a photon energy of 1.55 eV. Here a 1ω transition from $1s\sigma_g$ to $2p\sigma_u$ will be resonant at $R = 4.7$ au [7]. This is shown in the diagram as a portion of the wavepacket moving onto the 1ω-shifted $2p\sigma_u$ potential. Direct absorption of two photons is forbidden due to parity considerations, but dissociation can occur by absorption of three photons and subsequent emission of one photon, i.e. *net-absorption* of two photons. This is described as a transition onto the 3ω-shifted $2p\sigma_u$ potential (absorption of 3 photons, resonant at 3.3 au), followed by a jump back onto the 2ω-shifted $1s\sigma_g$ state (re-emission of one photon, resonant at 4.7 au). In both the 1ω and 2ω case, the coherent dissociative wavepacket continues to large R values along the respective potentials. On this trajectory the electron localises to one of the nuclei and at large R the molecule has fragmented to give $(D^+ + D)$, with the fragmentation energy shared between the products, and the D^+ is experimentally collected at the MCP detector.

In practice for the short (∼10–15 fs) intense pulses considered here, these dissociation processes are not restricted solely to transitions at the centre wavelength, as the wide bandwidth of the pulse permits absorption and subsequent re-emission to occur across the spectral profile. For example, a transform limited pulse with full-width at half-maximum (FWHM) duration of 13 fs and spectral profile centred around 800 nm, will have $\Delta\lambda = 100$ nm ~ 0.2 eV bandwidth across the pulse. For large enough photon flux (high intensities) this leads to an energy spread for 1ω and 2ω processes, rather than resonant peaks, which in turn means that a range of vibrational states from the $1s\sigma_g$ state can be accessed and hence contribute to the signal.

As a brief aside, it is worth noting that elsewhere this dissociation process has been described for longer pulse durations (∼50 fs) in the context of Floquet states [43–45] and 'avoided crossings' which open up around the resonant points in Fig. 3. This provides a 'cycle-averaged' picture of the distorted potential energy surfaces on which the nuclei evolve and is commonly referred to as 'bond-softening' [46]. This cycle-averaged interpretation provides a useful picture for explaining the range of vibrational states that are accessible, but is not strictly applicable for the pulse durations considered here, as the electric field (8/3 fs cycle) is no longer 'slowly-varying' with respect to the short pulse envelope of the order of 10 fs in duration (this slow-varying approximation is a key assumption in the Floquet approach).

So, the dissociating fragments will have a range of energies, depending on the photon energies absorbed and the vibrational states being accessed. The PD signal in Fig. 2 is in fact the sum of the 1ω and 2ω pathways, where it has been shown elsewhere that the separate contributions from each process can be estimated by fitting to the experimental spectra [47]. The 1ω process is manifested by the lower energy (later time) peak in the PD yield, with the 2ω process contributing to a 'shoulder' at higher energy (shorter flight time). Using linearly polarised light, any dissociating PD fragments will be projected along (or close to) the polarisation direction of the pulse [48] due to the alignment dependence of the coupling between the $1s\sigma_g$ and $2p\sigma_u$ states. This explains why no PD signal is observed in Fig. 2 when the pulse polarisation is perpendicular to the detection axis, as any fragments created from PD are projected perpendicular to the detection axis and thus lie significantly outside the aperture acceptance angle, for the geometry in Fig. 1. It is also apparent for polarisation parallel to the detection axis that the 'backward' PD peak exhibits less signal than the 'forward' peak. This is because any products projected away from the detector direction will experience a smaller acceptance angle than if they were projected towards the detector, simply because they have more time to execute lateral motion before being accelerated to the aperture by the extracting field.

[4] The energy of one photon is $\hbar\omega$ and this is equal to 1ω in atomic units of energy (Hartree). Although many of the diagrams in this report are annotated in eV (not Hartree), the $1\omega/2\omega$ notation is maintained for consistency with the general convention in the literature.

The signal denoted by 'CE' in Fig. 2 arises when the fragmentation channel is due to projection onto the repulsive Coulomb potential, i.e. a dissociative ionisation event where the molecule is stripped of electrons and results in two deuterons being detected. The kinetic energy release (KER) from this process is dictated by the Coulomb repulsion of the unshielded deuterons and this gives a higher fragmentation energy than the PD mechanism. The final appearance energy of a fragment will therefore communicate information about the internuclear separation at which this dissociative ionisation occurs (KER $\sim 1/R$). As with PD, this process may proceed via initial ionisation to the intermediate molecular ion D_2^+, which can then be sequentially followed by subsequent ionisation $D_2^+ \rightarrow D^+ + D^+$. This may occur instantaneously, leading to a direct Coulomb explosion of the D_2 target, or the D_2^+ wavepacket may move to larger R prior to this dissociative ionisation. For the data in Fig. 2 the lower bound of the fragment energy (3 eV) suggests that the molecule is projected onto the Coulomb potential at $R \leq 5$ au. Previous studies have suggested that if the molecule is allowed to begin dissociation and reach larger R values, there are resonantly enhanced dissociative ionisation processes occurring around 6 and 9 au [7], although these two separate points have not been explicitly observed experimentally [37]. This process is known as charge resonance enhanced ionisation (CREI) and it is a dominant mechanism for dissociative ionisation when the laser pulse is sufficiently long. However, recent studies [40,41,49] have shown that for the short pulses considered here (<15 fs) CREI is substantially suppressed as the expanding molecule does not have time to reach these larger R values in the presence of the laser field. As for PD, the CE process exhibits a strong alignment dependence along the axis of the laser pulse polarisation.

Although there is a significant probability that the CE process occurs via the D_2^+ intermediate, it can also occur as a direct, or non-sequential, process from D_2 via electron re-scattering or re-collision [51–55]. Here an electron, having been tunnel ionised from D_2 in the presence of a linearly polarised pulse, is accelerated by the laser field as it is projected away from the D_2^+ ionic core. Depending on the phase of the laser cycle at which the ionised electron is born, the oscillating electric field may drive the electron back towards the parent ion wherein it may collide with the residual molecule. From a simple classical trajectory calculation, the returning electron may possess a kinetic energy up to 3.17 U_p, where U_p is the ponderomotive energy (or 'quiver' energy) of the electron in the electric field of the pulse, given by

$$U_p = \frac{e^2 \mathcal{E}_0^2}{4m\omega^2}. \tag{1}$$

Here e and m are the electronic charge and mass respectively, ω is the angular frequency of the laser field and $\mathcal{E}_0$ is the peak value of the electric field amplitude. Taking the example of 800 nm radiation at 6×10^{14} W cm^{-2} ($\mathcal{E}_0 = 6.7 \times 10^{10}$ V m^{-1}), $U_p = 35.9$ eV and thus the energy of the re-colliding electron is sufficient to directly remove[5] the remaining bound electron (consider the energy scale in Fig. 3). This re-scattering mechanism occurs within a fraction of a cycle (~1 fs) and thus this is a Coulomb explosion event, in the true sense of the phrase, where the deuterons are suddenly unshielded at small R. This produces the high energy end of CE peaks in Fig. 2, arriving first at the detector. It is interesting to note that some re-collision products are observed even when the pulse is aligned perpendicular to the detection axis. This is because a molecule that is orientated in the plane of the detector may undergo a re-collision event and therein the fragments are projected in that plane by Coulomb repulsion of the deuterons, even if the laser pulse polarisation is perpendicular to the molecular axis.

Finally, it is clear that the interaction from the pulse aligned perpendicularly to the detection axis produces a peak around zero fragmentation energy. This corresponds to a process which is still under question. One possible explanation is 'bond hardening' or zero photon dissociation, where the molecule absorbs and re-emits photons across the spectral profile, thereby gaining enough energy to dissociate but giving up the remaining energy via radiative emission. Low energy fragments from this process will have a large acceptance angle, as they will not move significantly in the lateral direction in the time taken for vertical extraction. Also, in previous studies, this process has been shown to exhibit 'counter-intuitive alignment' [56] behaviour, where a measurable fragmentation signal is observed perpendicularly to the pulse polarisation.

In this section the ionisation and dissociation mechanisms of D_2 in short intense-field pulses have been outlined using typical experimental data. This provides the necessary platform for understanding recent advances in time-resolved studies to be discussed presently. Much of the remainder of this report will deal with investigation of bound wavepacket motion in the D_2 and D_2^+ molecules but first it is interesting to consider the dissociation of the D_2^+ molecule in a little more detail. In fact, with a minor modification to the experimental arrangement in Fig. 1, it is possible to study the temporal dependence of the ultrafast dissociation of this molecular ion.

4. Imaging D_2^+ dissociative wavepacket motion

It has been seen that a significant proportion of a coherent wavepacket created in D_2^+ can dissociate along the $1\omega/2\omega$ trajectories (shown in Fig. 3) without any further ionisation events. By applying a secondary pulse at some later time, it may be possible to remove the remaining electron from this dissociating system, projecting the dissociative wavepacket onto the repulsive Coulomb potential (as shown by the purple dashed arrows in Fig. 3). This would lead to an R-dependent fragmentation energy which is intrinsically linked to the timing of the secondary (probe) pulse. In this way, the evolution of the wavepacket in R will be tracked as a function of probe pulse delay time.

[5] The re-colliding electron may also lead to high harmonic generation (HHG) upon return to the parent molecule and this property has been innovatively used to probe small variations in nuclear motion during the timescale of the re-collision process [52,55].

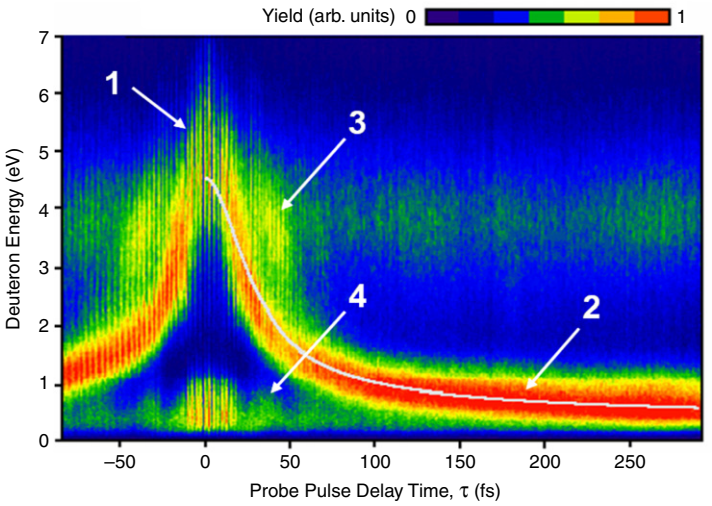

Fig. 4. Studies of D_2^+ dissociative wavepacket motion as function of pump-probe delay time, τ, through measurement of deuteron fragmentation energy. This example corresponds to two 5×10^{14} W cm^{-2} pump and probe pulses having linear polarisation vectors aligned parallel to the detection axis, with pulse durations of 15 fs. Interferometric effects around the pulse overlap are manifested as 'stripes' in the fragment yield near $\tau = 0$, indicated by arrow 1. Other highlighted features describe CE imaging of a dissociating wavepacket (arrow 2) and CE/PD imaging of a remaining bound wavepacket (arrows 3/4). The grey line is a simulated classical trajectory for a 1ω PD process. The results shown here are complementary to recent studies elsewhere [23,57–60].

Since initial studies by Trump et al. [57], this pump-probe scheme for studying the molecular breakup of D_2^+ through 'Coulomb explosion imaging' has been used by a number of research groups [23,58–60]. Such studies defined a significant first step in time-resolved imaging of nuclear dynamics in hydrogenic molecules.

In order to investigate the dynamics of a dissociating nuclear wavepacket using the experimental arrangement described in Section 2 (Fig. 1), it is helpful to align the pump pulse parallel to the detection axis. Dissociating fragments from the pump process will then be projected towards the detector. The time delayed probe pulse will ionise this dissociating system and therefore the Coulomb explosion of the dissociating system will return energetics which vary as a function of the pump-probe delay time, τ.

The results displayed in Fig. 4 are for such an experiment where both pulses have polarisations aligned parallel to the detection axis of the TOFMS. For positive delay times in Fig. 4, the variable arm of the interferometer acts as the pump pulse with the fixed arm providing the probe. The converse is true for negative delay times and the symmetric structure (about $\tau = 0$) of the energy spectra occurs because the pump and probe pulse parameters are identical. At small time delays (arrow 1) the pulses are temporally overlapped and the relative phase difference between their electric field cycles gives rise to constructive and destructive interference effects. The electric field ($\mathcal{E}_0$) associated with a peak laser intensity, I_0, is related by the cycle-averaged magnitude of the Poynting vector such that $I_0 = \frac{1}{2}\epsilon_0 c \mathcal{E}_0^2$ where ϵ_0 and c have their usual meanings.

So for two equal intensity pulses the constructive addition of the peak electric fields will provide four times the original intensity of a single pulse, resulting in a large fragment yield. Thus, at delay step intervals of one optical cycle near $\tau = 0$, the two pulses behave effectively as one strong pulse. Similarly at τ values where the pulses are out of phase with each other by half an optical cycle there is destructive interference with little or no fragment yield observed. Thus 'interference stripes' can be observed in the experimental yield. In the case of constructive interference, the D_2^+ wavepacket is created and projected directly onto the Coulomb potential curve at small R, with deuterons appearing with a maximum fragment energy upwards of 6 eV, as indicated by arrow 1 (consistent with the projection of a wavepacket at small R in Fig. 3). These interference effects are complementary to observations made by Ergler et al. [23,58] and Alnaser et al. [60,61] in this type of experimental study. The overlapped pulse around $\tau = 0$ also gives rise to direct observation of 1ω and 2ω PD products with energies in the range 0–1.5 eV. Here, the overlapped pulse ionises the target and subsequently creates a dissociating wavepacket in D_2^+. As seen previously, the separate 1ω and 2ω channels are not resolved from each other because the non-resonant processes each access a range of vibrational states, contributing to overlapping energy distributions from these two channels.

The red band of fragmentation signal which shifts from high energy to low energy as τ increases (indicated by arrow 2) is the CE imaging of the PD channels. The deuterons from this fragmentation sequence gain energy from both the initial (pump pulse) PD process (E_{PD}) and the subsequent (probe pulse) CE imaging kinetic energy release, such that the observed energy per dissociating fragment is given (in au) by

$$E_{fragment} = \frac{1}{2}\left(E_{PD} + \frac{1}{R}\right). \tag{2}$$

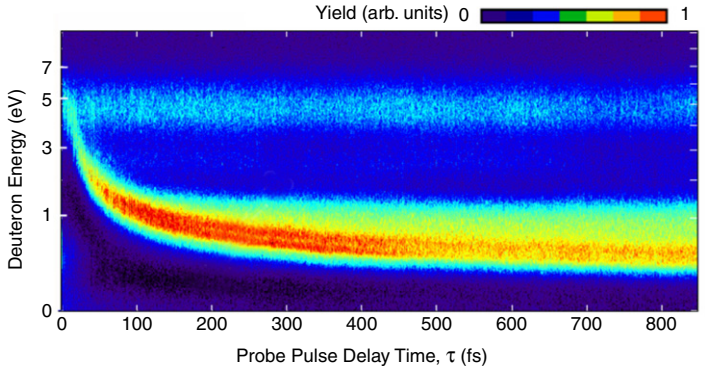

Fig. 5. Isolated observation of a D_2^+ dissociative wavepacket. By aligning a pump pulse (15 fs, 5×10^{14} W cm^{-2}) parallel to the detection axis, a dissociating wavepacket is initiated along this direction. A probe pulse (in this case 15 fs, 7×10^{14} W cm^{-2}) will remove the remaining electron to cause Coulomb Explosion of the dissociating system. If the probe pulse polarisation is aligned perpendicular to the detection axis, it does not contribute significant signal from single pulse interactions (ionisation or dissociation) or from sampling of a bound wavepacket.

At small τ values, the wavepacket is at small R when probed and the CE channel imposes a high kinetic energy release. For larger values of τ, the wavepacket reaches large internuclear separations prior to being imaged and the removal of the final electron releases less kinetic energy, as the Coulomb repulsion has become less significant. So, as τ increases, the CE energy tends towards zero and the asymptotic limit of the shifting red band tends to the PD energies seen around $\tau = 0$. The grey line in Fig. 4 is a predicted classical trajectory [23,57,60] for a 1ω dissociation process with final fragment energy set at 0.34 eV, corresponding to the mean 1ω appearance energy experimentally observed for a single pulse process [47] (using a time-of-flight spectrum, similar to Fig. 2, for the pump pulse in this experiment). In this simple simulation the path of a fragment along the dissociative channel has been classically modelled and then projected onto the Coulomb curve at each τ value, resulting in good agreement with the experimental data.

The main features in Fig. 4 are clearly representative of dissociative effects but there are also signatures of bound wavepacket motion. Here, the pump pulse ionises the D_2 target molecule to create a coherent bound wavepacket in the $D_2^+ 1s\sigma_g$ potential. At around 34–38 fs the bound wavepacket has executed ~1.5 vibrational periods and (as will be discussed in more detail later) is mostly in phase near the 1ω and 2ω crossings. At this τ value an enhanced signal is therefore observed in the PD channel (arrow 4). This PD imaging of the bound wavepacket is not clearly resolved beyond $\tau = 100$ fs due to the dominant structure of the CE imaged dissociative wavepacket (arrow 2). A similar enhancement effect is seen in the CE channel (3–5 eV), as indicated by arrow 3, but the structure disappears at later times as the wavepacket de-phases [25,60], for a full discussion see Section 5. It should be noted that some of the signal in the CE channel may arise from a direct one pulse process, where a D_2 target can undergo sequential ionisation giving fragments of energy 3–5 eV. However, the enhancement around 34–38 fs clearly represents probing of bound motion and this de-phasing effect is a fundamental property of the quantum nature of the bound wavepacket.

In order to isolate observations of either solely bound or solely dissociative wavepacket motion, the polarisation effects observed in Section 3 may be used to full advantage. First, in order to focus on dissociative effects the pump pulse may be orientated parallel to the detection axis, to initiate the PD, and it is then beneficial to probe perpendicularly. This will create detectable Coulomb explosion fragments by removal of the final electron and for high enough probe intensities no direct PD events will be observed at the detector. This is because all initial PD processes from the pump are probed via CE and any PD processes from the probe are perpendicular to the detector and will not be measured (see Fig. 2).

Results for this configuration of pulse polarisations are shown in Fig. 5. The shifting band clearly shows that the probe pulse induces the CE imaging of the dissociating wavepacket initiated by the pump. The high energy contribution of CE fragments is essentially invariant as a function of τ and therefore due to direct single pulse processes from either the pump or the probe, consistent with those observed in Fig. 2. It is fascinating to note that there is no direct PD signal at short delay times, verifying that the probe pulse ionises *all* of the dissociating D_2^+ created by the pump pulse and that all of the detected PD signal is from the imaging of the dissociative wavepacket. There is even a slight splitting of the band of signal corresponding to CE imaging of dissociation, suggestive of a resolution between 1ω and 2ω channels.

The polarisation orientations used here therefore provide a method for isolated detection of ultrafast dissociative D_2^+ wavepackets. These observations are consistent with recent studies reported elsewhere [23,57–60]. It is worth noting that the COLTRIMS technique [17] was used by Ergler et al. [23] to make the first highly-resolved observations of D_2^+ dissociation in this way, however there are also significant benefits to the simple TOFMS method, as purely dissociative wavepacket dynamics can be isolated and the observations do not suffer from some 'false coincidences' which can occur in COLTRIMS experiments. With reference to features 3 and 4 of Fig. 4, it is now interesting to consider how bound wavepacket motion may be isolated and studied.

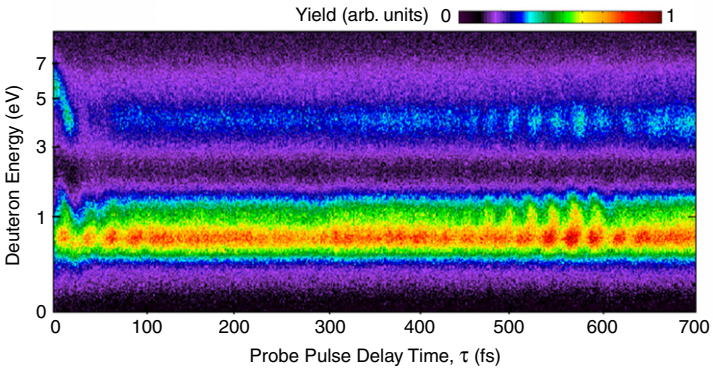

Fig. 6. Experimental imaging of bound vibrational wavepacket motion in D_2^+, using 13 fs pump (8×10^{14} W cm^{-2}) and probe (6×10^{14} W cm^{-2}) pulses. The deuteron (D^+) energy spectra is shown as a function of pump-probe delay, τ, and displays clear vibrational 'de-phasing' and 'revival' effects in PD (0.5–1.5 eV) and CE (3–6 eV) channels in the 0–50 fs and 500–600 fs regions respectively. The colour scale represents the deuteron yield in scaled ('arbitrary') units where the peak yield corresponds to 1.0.

5. Bound vibrational wavepacket dynamics in D_2^+

In order to study bound vibrational dynamics in D_2^+, a further adjustment can be made to the experimental arrangement. By orientating the pump pulse perpendicular to the detection axis, bound D_2^+ ions may be created. Any fragments from dissociation events induced by this pulse will move perpendicular to the detector axis and can therefore be disregarded. A probe pulse parallel to the detection axis will then sample the bound D_2^+ wavepacket, creating D^+ products via PD and CE. The results from this type of experiment are shown in Fig. 6, displaying a well resolved energy spectrum detailing both CE (3–6 eV) and PD (0–1.5 eV) imaging of the coherent bound D_2^+ wavepacket. Feature 2 of Fig. 4 has clearly been avoided, effectively removed from the detection arrangement due to the pulse polarisation orientations.

The primary feature in the colourmap is the striking enhancement in the PD channel from 0–50 fs and again from around 500 fs onwards, both of which can be clearly seen in the oscillating structure of the integrated yield of the PD signal in Fig. 7 (c). Since the PD process occurs at R values near the outer turning point of the $1s\sigma_g$ potential well (see Fig. 3), it serves to sample the bound wavepacket near this point. Similarly the CE channel is enhanced at large R. It is worth noting that, in principle, the CE channel could provide a mapping of the wavepacket across the full width of the potential well, but this would require significantly higher intensities in the probe pulse. With typical pulse intensities, the CE channel is subject to an R-dependent probability, which dictates an enhancement at larger R values.

Thus the peak structures in the PD and CE integrated yields in Fig. 7 correspond to the wavepacket being localised at large R and the troughs correspond to the wavepacket being localised at small R values. The D_2^+ yield is conversely modulated, it is depleted when CE and PD are peaked and it peaks when there is a trough in CE and PD yields. What is fascinating here is that there are only specific time windows where this oscillatory behaviour is observed, the oscillating structure around 500–600 fs is the so-called *wavepacket revival* and will be discussed presently.

When the pump pulse ionises the D_2 target, the resulting wavepacket launched on the $1s\sigma_g$ surface of D_2^+ may be expressed as a coherent superposition of D_2^+ vibrational eigenstates, ϕ_v, each with associated frequency $\omega_v = E_v/\hbar$ (where E_v is the energy of the vibrational level). This may be expressed as:

$$\Psi(R, t) = \sum_v a_v \phi_v \exp\{-i\omega_v t\}. \tag{3}$$

In the wavepacket, the exact vibrational distribution (distribution of a_v values) is dictated by the nature of the pumping process, which is sensitive to pump-pulse intensity, duration and polarisation and exhibits a rate dependence on the internuclear separation [63–65]. It should therefore be noted that the pump process is not a universal function and, as discussed in [66], the pulse parameters must be carefully considered when simulating experimental conditions. It is instructive to observe that in some recent experiments [24,67] where pump pulses of 10–15 fs, 5–8 $\times$ 10^{14} W cm^{-2} have been used to initiate coherent vibrations, subsequent wavepacket evolution has been well reproduced by a Franck–Condon (FC) distribution [68].[6]

[6] As a brief aside, it is worth highlighting that in these experiments the polarisation vector of the linear pump pulse was effectively aligned perpendicular to the molecular bond axis. In contrast to this, in other recent studies the pump polarisation was aligned parallel to the internuclear bond axis and results were observed to deviate from an FC distribution. Indeed in the work of Niikura et al. [69], Ergler et al. [70] and Rudenko et al. [71] the requirements for non-FC distributions are discussed and invoked. This appears to be consistent with a trend observed in [63] which predicts a narrow vibrational distribution (few states) for polarisation parallel to bond axis and a broader distribution (more states populated) for the perpendicular configuration. In this context, an FC transition is used here to model the pump pulse, i.e. for specific conditions similar to [24,67], and hence to initiate the D_2^+ vibrations.

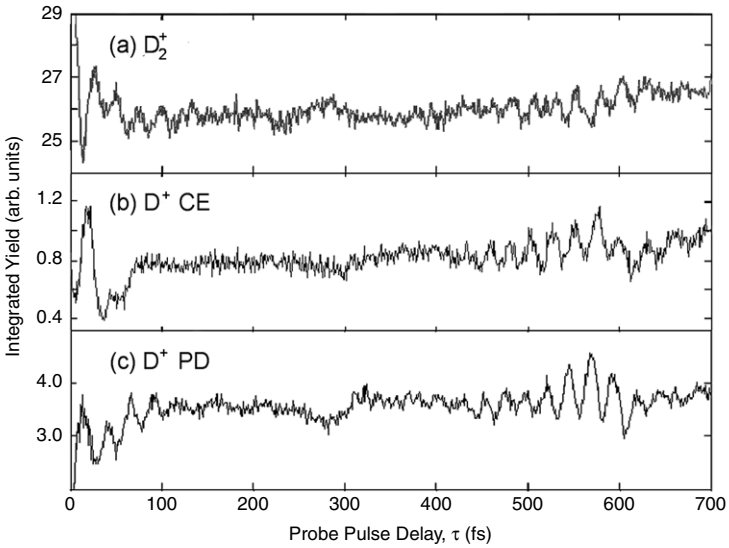

Fig. 7. Integrated yields for (a) D_2^+, (b) CE and (c) PD channels corresponding to the experiment in Fig. 6, i.e. (b) and (c) are the integrals of the upper and lower energy bands respectively in Fig. 6. The oscillations from 500–600 fs are signatures of the wavepacket revival, where the wavepacket is executing well defined motion back and forth across the $1s\sigma_g$ potential. Peaks (or dips) in CE and PD infer that the molecule is at its outer (or inner) turning point in R. The D_2^+ yield is conversely modulated.

In the FC approximation, the vibrational superposition is created by projection of the D_2 $v = 0$ wavefunction onto the D_2^+ $1s\sigma_g$ potential. In this case, the amplitude a_v is given by the overlap integral between the initial D_2 $v = 0$ state and the D_2^+ eigenstate v. At a given time t the probability density of the wavepacket can be shown to be:

$$|\Psi(R,t)|^2 = \sum_v |a_v|^2 |\phi_v|^2 + \sum_{v,v' \neq v} a_{v'} a_v^* \phi_{v'} \phi_v^* \exp\{-\mathrm{i}(\omega_{v'} - \omega_v)t\}. \tag{4}$$

The first term in Eq. (4) is a temporally invariant summation of standing waves. The $|a_v|^2$ values are the relative populations of each state and in this case provide meaningful contributions over ∼10 vibrational states. In this representation, it is the second term that provides the time dependent dimension to the motion. At $t = 0$ the exponential term is unity for all terms in the summation, however as time evolves this expression is dictated by the interference terms between separate vibrational levels. The probability density will deviate from its original form, dependent on the frequency spacings between the separate eigenstate components, where $\omega_{v',v} = \omega_{v'} - \omega_v$ are the 'beat' frequencies dictating the time dependent motion. In a classical analogy, the system may be regarded in a similar way to an ensemble of molecules vibrating at different quantised frequencies. For example, each level can be approximated to vibrate with 'classical frequency' $\omega_{v',v}$, where $v' - v = 1$ and the separate levels go in and out of phase with each other. In reality, the quantum nature of the system is more involved and subtle, with higher order beat contributions from $v' - v = 2, 3 \ldots$ but this classical analogy is nonetheless a useful picture to understand the system to a first approximation.

Results from a quantal simulation of the bound wavepacket motion are displayed in Fig. 8. This particular simulation can be simply carried out by calculating the eigenstates ϕ_v and eigenvalues ω_v of the time independent Schrödinger equation for both D_2^+ and D_2 on a finite difference grid using accepted values for the ground electronic state potentials [73]. The ground vibrational eigenstate in D_2 is used to find the a_v values, within the FC approximation, by the overlap integral with each ϕ_v in the D_2^+ ion. Eq. (3) can be evaluated as a function of time and the probability density, $|\Psi(R,t)|^2$, obtained. The colourmap describing this motion is displayed in Fig. 8(a), with the colour scale representing the probability density. The expectation value of the internuclear separation ($\langle\Psi|R|\Psi\rangle$), has been calculated for this wavepacket and is shown in Fig. 8 (b). Furthermore, the autocorrelation function, $|\langle\Psi(R, t = 0) \mid \Psi(R,t)\rangle|$ measures the overlap of the wavepacket at time t with the initial wavepacket, and the square of this is shown in Fig. 8(c). (For more detailed discussions on such calculations and wavepacket dynamics, the reader is referred to the instructive article by Feuerstein and Thumm [74] which served to instigate much experimental work in this area.)

For the simulation shown here, it can be clearly seen in the colourmap that the wavepacket starts at small R and initially moves in phase towards larger R values, where some of the higher lying vibrational eigenstates contribute to the motion above 5 au. However, during subsequent oscillations the separate eigenstate contributions begin to de-phase with respect to each other and thus the motion becomes delocalised and spreads across the range of R values. As seen in Eq. (4), this is due to the de-phasing of the different vibrational beat frequencies $\omega_{v',v}$. This de-phasing effect can also be observed in the expectation value of the wavepacket. The initial well defined oscillation recedes after 70–80 fs with the expectation of the wavepacket position in R tending towards a mean value in the centre of the $1s\sigma_g$ well.

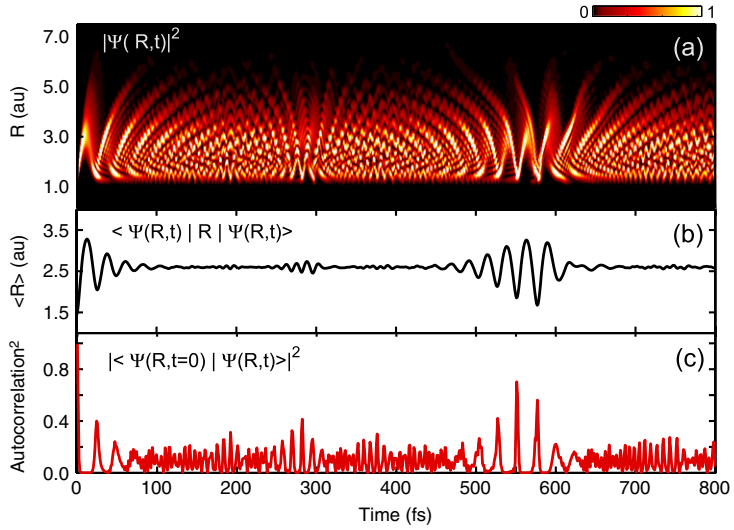

Fig. 8. Simulation of vibrational wavepacket motion in D_2^+, consistent with [74]. (a) Probability density of wavepacket as a function of time. The colour scale is shown in relative units (0–1) where 1 is assigned to the peak of the probability density. (b) Expectation value of the wavepacket position in R. (c) The square of the autocorrelation function, which calculates the overlap of the wavepacket at time t with the initial wavefunction $\Psi(R, t = 0)$.

As the wavepacket motion progresses over hundreds of femtoseconds, many components of the vibrational wavepacket begin to re-phase with each other around the same time, culminating in the distinct 'revival' [62][7] structure centred around the region 500–600 fs. Here the colourmap displays clear diagonal stripes where the wavepacket seems to execute well defined motion back and forth in R. This is confirmed by the expectation value which regains a clear oscillatory structure within this time window, i.e. the wavepacket is moving in phase and as a localised packet as it oscillates back and forth across the $1s\sigma_g$ potential well. At this vibrational revival, the wavepacket has almost returned to its original form, as evidenced by Fig. 8(c) which shows the autocorrelation function at 553 fs exhibiting a peak value. It should be noted that, since the complete set of vibrational states in the D_2^+ ion are not all exactly in phase at this point, the autocorrelation is not exactly equal to one and hence the revival is not a complete replica of the initial system conditions.[8]

So, the vibrational revival presents a time window where the wavepacket oscillates in phase between outer and inner turning points. As stated, the peak structures in the PD and CE integrated yields (in Fig. 7) correspond to the wavepacket being in phase at large R and the troughs correspond to the wavepacket being in phase at small R values. These channels therefore provide clear imaging of the wavepacket revival.

For optimum conditions it has been shown [70] that the CE channel also returns R-dependent imaging signatures (via kinetic energy release) and this can be used to deduce spatial as well as temporal ('spatiotemporal') imaging of the wavepacket. In particular, the R-dependence of the vibrational wavepacket may be considered and used to extract spatial and temporal information about the eigenstate contributions [75,76], as will be discussed in due course.

In the present simulation, another interesting feature can be seen in Fig. 8 at around 275 fs, where the autocorrelation and expectation value exhibit a mini revival structure. Indeed, similar implications are seen in the colourmap with this 'fractional revival' occurring, with half the period of the revival at 550 fs. The fractional revival may be understood as two sub-wavepackets propagating across the potential, exactly out of phase with each other.[9] Thus at half a 'classical' vibrational period one of the sub-wavepackets is overlapped with $\Psi(R, t = 0)$, giving a small peak in the autocorrelation. In the colourmap it is interesting to observe that this fractional revival is also the turning point between de-phasing and re-phasing patterns in the wavepacket motion, with a symmetry occurring around this point. However, this structure is not directly observable in the experimental results since the duration of the probe pulse is on a comparable timescale to the ∼12 fs oscillations. Moreover, the coherence of the initial wavepacket created by the pump pulse will dictate that the motion will not be as well defined as the simulations, where the wavepacket is assumed to start instantaneously in a FC distribution.

[7] For the nomenclature used in the seminal work of Robinett [62], this can strictly be characterised as a 'half-revival', where the eigenfunctions are in-phase at the outer turning point of the $1s\sigma_g$ well. The corresponding 'full-revival' occurs at twice this time when the rephasing occurs at the inner turning point [108], however at both 'half' and 'full' revival times the vibrational dynamics are alike, where the wavepacket executes localised oscillations in R.

[8] Further revivals may also occur at later times but it follows that these future revivals (at 1100 fs, 1650 fs …) will exhibit less pronounced structures as the frequency components will re-phase a little less each time. This is not to say that the wavepacket has lost coherence, just that the phases of eigenstates are such that the coherence is not observed through a dramatic revival structure at these particular times. Indeed at much later times, the states rephase again and the revival structures will be recovered, culminating in a so-called super revival [62].

[9] In fact at this fractional revival the even eigenstates are all in phase with each other and exactly out of phase with the odd eigenstates (also in phase with each other).

This will be discussed in Section 7. Nonetheless, the experiment is well described and the physics well explained by the simulations shown here.

Finally, with this qualitative agreement at hand for the simulated and experimentally obtained revivals, it is also interesting to observe the similarities between the expectation value in Fig. 8(b) and the PD/CE yields in Fig. 7, displaying clear correlation between the imaging signals and the evolution of the wavepacket in the internuclear separation coordinate. However, in order to more directly compare experiment with theory, the imaging process itself must be simulated.

6. Modelling the probe pulse: Photodissociation

To provide extra insight into the quantum dynamics being studied in these pump-probe experiments, time-dependent quantum modelling can be used to simulate not only the wavepacket motion (in Section 5) but also the effect of the probe pulse [47,75,76]. For these pulse durations, at intensities $\leq 2 \times 10^{14}$ W cm^{-2} photodissociation is significantly the dominant fragmentation pathway [77]. Whilst imaging via the CE channel can also provide useful characterisation of wavepacket dynamics and will be discussed in more detail in due course, it will be seen in this section that the quantum modelling of the PD channel provides significant insight into wavepacket dynamics and molecular breakup. One example of such a model will be discussed here, where the vibrational wavepacket is initiated and propagated on $1s\sigma_g$ and the application of the probe pulse is simulated by laser-induced coupling of electronic states in D_2^+, leading to photodissociation.

For this technique, the wavepacket is typically represented on a finite difference grid in R, composed of 1000 points spanning 20 au. At $t = 0$ the wavepacket can be simulated (within the FC approximation) by the ground vibrational eigenstate of the D_2 molecule on the $1s\sigma_g$ potential of D_2^+. The subsequent propagation within the TDSE is modelled via the time-evolution operator, where two popular numerical representations are the split-step algorithm [78,66] and Taylor series expansion (e.g. [79]). Within the Taylor series expansion technique the wavefunction at time $t = t_0 + \Delta t$ can be given by,

$$\Phi(R, t_0 + \Delta t) \approx \mathrm{e}^{-\mathrm{i}H(t_0)\Delta t}\Phi(R, t_0) \approx \sum_{k=0}^{k=N} \frac{(-\mathrm{i}H(t_0)\Delta t)^k}{k!}\Phi(R, t) \tag{5}$$

where $H(t)$ is the Hamiltonian for the nuclear system. This expansion is generally evaluated up to $N = 8$, for convergence in simulations. If a time independent Hamiltonian is used then this technique will retrieve the same results as Fig. 8, where the field-free motion of the wavepacket is tracked on the $1s\sigma_g$ potential. However the advantage to using this type of propagator is that the application of the probe pulse can be modelled by including a time-dependent coupling in the Hamiltonian, between the groundstate ($1s\sigma_g$) and the excited level ($2p\sigma_u$). For the D_2^+ molecule these two states are significantly isolated from any higher lying states such that, at the laser intensities considered here, the coupling effect need only be considered between these two levels.

The coupling[10] is given by $\Omega(R, t) = -d(R).\mathcal{E}(t)$, where $\mathcal{E}(t)$ is the electric field from the laser pulse (oscillating with the optical laser frequency) and $d(R)$ is the dipole moment of two-state system given by

$$d(R) = \frac{R}{2\sqrt{1-p^2}} - \frac{1}{2 + 1.4R} \tag{6}$$

where $p = (1 + R + R^2/3)\,\mathrm{e}^{-R}$, (see [80,81]). The time-evolving electric field profile of the laser pulse, $\mathcal{E}(t)$, can be defined, within the dipole approximation, as

$$\mathcal{E}(t) = \mathcal{E}_0 \exp\left(-\frac{2\ln 2(t-\tau)^2}{W^2}\right)\cos\left\{\frac{2\pi c}{\lambda}(t-\tau)\right\}. \tag{7}$$

Here the envelope of the pulse is a Gaussian profile centred at a chosen delay time τ and the profile is modulated by a carrier field oscillation at the central frequency of the pulse, represented by the cosine term. The FWHM of the pulse in the *intensity profile* is given by W. Note that this intensity measure of FWHM is used here as it is a typical parameter obtained experimentally, corresponding to $W\sqrt{2}$ fs in the electric field Gaussian profile ($I \propto \mathcal{E}^2$).

For a 1-D model (in R) with the laser field acting along the molecular bond axis, the nuclear motion of the system can be described by two coupled equations given by

$$\begin{aligned} -\frac{1}{2\mu}\frac{\partial^2}{\partial R^2}\Phi_g + V_g(R)\,\Phi_g + \Omega(R, t)\Phi_u &= i\frac{\partial}{\partial t}\Phi_g \\ -\frac{1}{2\mu}\frac{\partial^2}{\partial R^2}\Phi_u + V_u(R)\,\Phi_u + \Omega(R, t)\Phi_g &= i\frac{\partial}{\partial t}\Phi_u \end{aligned} \tag{8}$$

[10] For the conditions considered here, the coupling can be modelled using the electric field of the pulse and no quantisation of the light field is necessary. This is because the high photon flux (high intensity) and low photon energies (compared to the transitions) mean that the process is well modelled within a semi-classical strong field approximation.

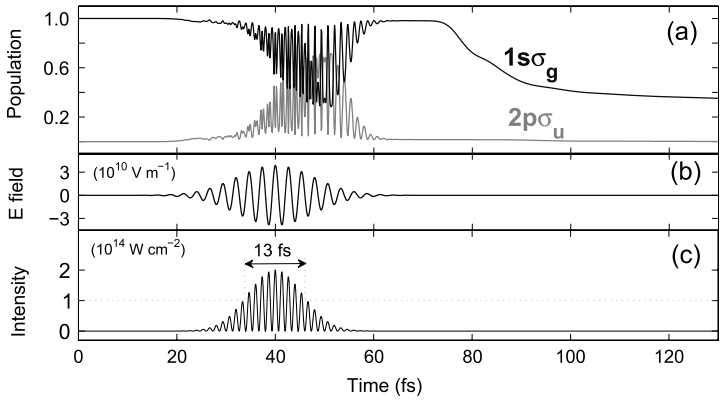

Fig. 9. Two state coupling calculation to simulate the probe pulse at 40 fs delay for a 2×10^{14} W cm^{-2} pulse with $W = 13$ fs. (a) Rapid population transfer and subsequent loss (dissociation) of $1s\sigma_g$ wavepacket. (b) Electric field profile of the pulse used in the coupling term in Eq. (8) and (c) the corresponding intensity profile.

where μ is the reduced mass of the system, Φ_g, Φ_u are the temporally evolving wavefunctions on $1s\sigma_g$ and $2p\sigma_u$ potentials respectively and V_g, V_u are respective values of the potentials [73]. Numerical details for this type of scheme can be found elsewhere [47,82], where the equations can be discretised and the second order differential term can be expressed using adjacent terms on the finite difference grid. The Taylor propagator in Eq. (5) can then be used to calculate the time evolution of the wavefunctions Φ_g, Φ_u in Eq. (8).

For the results displayed in Fig. 9, the pulse characteristics were chosen to give a good representation of typical experimental parameters. It is clear that the pulse dictates the strength of the coupling term in Eq. (8), which acts to transfer population between the two electronic levels and can occur across the bandwidth of the laser by absorption and re-emission of many photons. For the probe delay time at 40 fs the population of the $1s\sigma_g$ potential can be seen to be transferred onto the $2p\sigma_u$ state, with portions of the wavepacket subsequently oscillating back and forth at the frequency of the optical field. Initial transitions from the bound $1s\sigma_g$ state do not occur until the coupling is significantly high (strong electric field) and after this many rapid oscillations occur.[11] As described in Section 3, the wavepacket may then proceed out to large R on either the $2p\sigma_u$ or $1s\sigma_g$ states by net 1ω or 2ω processes respectively. In the model any population reaching out to a chosen R value is multiplied by a masking term to simulate dissociation, and the simulation thus retains only the bound population on the $1s\sigma_g$ curve. For example, at around 70 fs most of the wavepacket is still on the $1s\sigma_g$ potential, some is bound and some is starting to dissociate. At 85 fs about half of the $1s\sigma_g$ population has passed 12 au and has been removed from the simulated $1s\sigma_g$ population by the mask term, showing around 50% dissociation. For the data in Fig. 9(a), the final population of the $1s\sigma_g$ state is around 36%, wherein 64% of the population has dissociated.

For this particular probe pulse delay time, it is clear that most of the dissociation occurs on $1s\sigma_g$, i.e. by 2ω process. The channel for dissociation (1ω or 2ω) varies as a function of probe delay time and this has been used elsewhere [47] to demonstrate the control of the dissociation pathway. However, with respect to the pump-probe studies under consideration here it is only necessary to consider the dissociated signal (e.g. 64% for a 40 fs delay).

To provide comparison with experiments, this dissociation calculation can be carried out for a full range of probe times from 0 to 700 fs, with the resulting dissociated signal at each time plotted in Fig. 10(b). This shows a predicted experimental yield for PD imaging of the bound D_2^+ wavepacket. The general trend of this model is remarkably consistent with the experimental data, which is plotted for comparison in Fig. 10(a). Also plotted is a 'critical R cut-off' (CRC) approximation to the PD yield [82], shown in (c). This is a simple technique used for predicting the dissociation of the wavepacket, for a probe centred at delay time τ. It is executed by approximating that all wavepacket above a critical R (at the time corresponding to the centre of the laser pulse) can be assumed to dissociate. That is, the wavepacket is simply 'cut-off' above this critical R value. The cut-off point is estimated by comparison with the full quantum simulation, and for a 13 fs, 2×10^{14} W cm^{-2} probe pulse the critical R value at 2.4 au provides excellent agreement with the intensive quantum simulation. The remarkable similarity between the full simulation and this simple model extends across all delay times and verifies that the PD process, at its core, can be simply described as a sampling of the wavepacket at large R values.

More importantly, the de-phasing and revival regions in the simulations are also temporally very consistent with the experimental data. This is most clearly seen around the revival region where the temporal separation and position of the peaks in the integrated yield are extremely well reproduced. Both the simulated and experimentally observed revivals display asymmetric characteristics wherein the structure begins to slowly build up from around 430 fs until the main peak at around 570 fs and then the wavepacket de-phases comparatively quickly, within about 50 fs, due to the broad distribution of states.

[11] The interested reader can find out more about these oscillations between the electronic states and how they can be used to vibrationally manipulate the molecule in some recent theoretical studies [66,79,82–84].

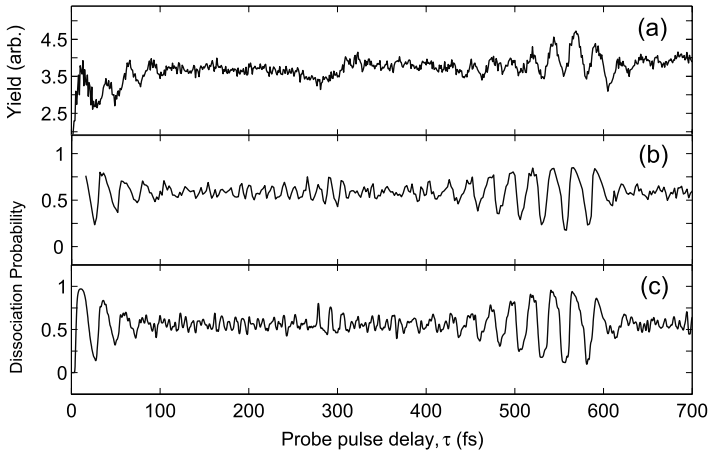

Fig. 10. (b) Quantum simulation of the photodissociation channel, providing the expected fractional yield (probability of dissociation) as a function of pump-probe delay time. This example was carried out for a 13 fs, 2×10^{14} W cm^{-2} probe pulse. The experimental yield from the PD channel (reproduced from Fig. 7) is shown in (a) for comparison across a full range of τ delay times. Striking similarities are apparent in the temporal dependence and structure. (c) The CRC approximation [82] provides a convenient method for reproducing the PD structure without using intensive computer simulations, in remarkable agreement with (b).

However, it is also clear that the absolute amplitude of the revival is more enhanced in the model than in the experiment. This may be due to using a purely two-state approach where imaging is only via dissociation and does not include the CE process, which is a competing channel. Perhaps more likely is that the discrepancy between theory and experiment is connected to coherence effects, as will now be discussed.

7. Photodissociation probing of vibrational wavepacket coherence

For the purposes of modelling the vibrational wavepacket, so far in our discussion it has been assumed that it is created instantaneously, with no effect of the pump pulse duration accounted for. If the wavepacket is initiated over some time window, the wavepacket will not be so finely resolved and if indeed the pump pulse was to exceed the vibrational timescale it will tend towards an incoherent superposition of states [74].

For the wavepacket in a single molecule, this means that the ionisation event projects the D_2 wavefunction onto the D_2^+ $1s\sigma_g$ surface in a well defined, narrow time window. For an instantaneous transition, the resulting wavepacket is given by Eq. (3) and this has been used in the wavepacket simulations demonstrated so far. If the production of the wavepacket is integrated over some time T (i.e. many ionisation transitions occurring at times between 0 and T) then the wavepacket expression can be written (as shown in [74]) as

$$|\overline{\Psi(R,t)}|^2 = \sum_v |a_v|^2 |\phi_v|^2 - \sum_{v \neq v'} a_{v'} a_v^* \phi_{v'} \phi_v^* \left(\frac{\exp\{-\mathrm{i}\omega_{v',v} T\} - 1}{\mathrm{i}\omega_{v',v} T} \right). \tag{9}$$

This arises from a simple integration where an equal weighting is given to the pump pulse contribution at each step in the integral from $0 \rightarrow T$. Thus the expression is for illustrative purposes only and is not a detailed model for the actual pumping process. For $T \gg 1/\omega_{v',v}$ the exponential term goes to 1, the time dependent term becomes negligible and the wavepacket tends towards a temporally invariant set of standing waves.

In experimental studies, an ensemble of molecules is studied and the experiment is repeated many times. So the wavepacket coherence condition can be interpreted in this context; all the target molecules must be ionised within a well defined narrow time window, beginning their outward motion from small R in tandem with each other. If a large number of D_2^+ ions were created across a timescale much longer than the vibrational timescale, then on average such an ensemble would not move coherently as there will always be some ions at each position in R. Hence for large pulse durations, Eq. (9) would provide a wavepacket description for the effectively incoherent ensemble of molecules.

Although Eq. (9) offers some measure of timescales required for coherence, a more quantitative and practical insight can be gained by experimentally varying the pump pulse duration. This can be done by placing fused silica slides in the path of the pump pulse and hence, by varying the slide thickness, pump pulse durations can be varied. The probe pulse can be kept fixed and the coherence of the wavepacket can be investigated through observing the subsequent revival structure that is imaged, as shown in Fig. 11(c). The experiment shows that as the pump duration increases, the wavepacket coherence is lost and for longer pump durations, the vibrational revival structure is not observable.[12]

[12] The resulting structure is not however a flat, monotonic signal but still displays a 'slow' (compared to vibrational timescales) modulation as a function of probe delay time. This is actually an underlying signature of a rotational motion, to be discussed in due course. For the present, it is sufficient to note that this 'slow' modulation does not cloud the clear vibrational dynamics in these experiments.

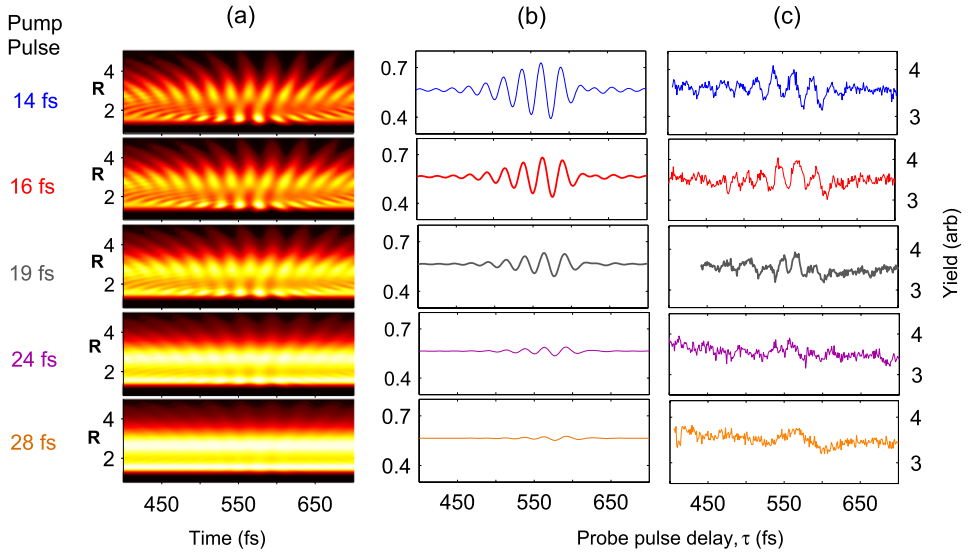

Fig. 11. Effect of pump pulse duration on wavepacket coherence. The probability density colourmaps in column (a) have been averaged over Gaussian profiles to give a rough simulation of the pump pulse duration, using a colourscale consistent with Fig. 8. Subsequently, the cut-off approximation has been used to predict corresponding PD yields in column (b). Column (c) displays data around the revival for experiments similar to Fig. 7, where the pump was varied and the probe was fixed at 13 fs.

In order to provide a comparison with theory, it is not trivial to fully model the exact nature of the pump pulse. Let us consider a few key constraints here. If the pump pulse occurs over a time window, then at some start time a wavepacket portion will be projected from $D_2 \rightarrow D_2^+$ and begin to oscillate. Some Δt later another projection of D_2 ($v = 0$) may occur, and so on. However, when this projection happens, the portion of wavepacket on the D_2^+ surface will also be experiencing the laser pulse and this must be modelled. Not only this, but the projected wavefunction will also have a different phase depending on the time of projection, due to the evolution of the phase of the D_2 ($v = 0$). In addition to this, for particular pulse parameters (especially $<10^{14}$ W cm^{-2}) the R-dependence of the ionisation rate becomes important [64] and this would have to take into account a range of plausible intensities within the focal volume of the laser. Suffice to say this is a considerable task to model and, although some studies have considered the R-dependence [63,64,83,65,85] for certain pump pulse parameters, the pumping process has not been comprehensively addressed in any current literature on ultrafast time-resolved studies of wavepacket dynamics.

For the data in Fig. 11 the pumping process has been treated, as a first approximation, to be an FC transition weighted over a Gaussian temporal profile, with FWHM corresponding to the pulse durations in the experimental studies. The resulting probability densities can be seen in Fig. 11. In this rough approximation, the 14 fs pulse is simulated to create a coherent wavepacket, where clear oscillations are still seen around the revival time. In the other extreme, the 28 fs probability density is almost completely invariant with time and is largely just the incoherent summation of standing waves from the first term in Eq. (9).

The resulting dissociation yield can be simulated for these probability densities. In keeping with the probability density maps, the cut-off yield can be seen to lose coherence as the pumping pulse is averaged over longer durations, and no significant wavepacket oscillation is expected for a 28 fs pulse. So this simplified model, for both pump and probe pulses, provides good agreement with experiment and it is clear that the wavepacket coherence has been manipulated in the experiment. Although the precise nature of the pumping process has not been characterised in detail, it is clear that for pulse durations $>$ vibrational timescales (of the $\Delta v = 1$ beats), any D_2^+ ion will be created in an *incoherent* distribution of vibrational states.

These results are consistent with [24,25,72], which show that it is only these pulses of sub-vibrational duration which enable the vibrational dynamics to be resolved. For even shorter pulse durations the wavepacket will become even better resolved and tend to the instantaneously created wavepacket in the simulations shown in Fig. 10.

As seen from the experimental results shown here, it is clear that coherent wavepacket studies are dependent on sub-vibrational interactions to initiate the wavepacket in a short (preferably 'instantaneous') time window, to enable the dynamics of the broad distribution of states to be tracked.

8. Modelling the probe pulse: Coulomb explosion

For the experimental results that have been shown in this article, photodissociation is clearly the main imaging channel, since it delivers much higher yields than the Coulomb explosion channel. Thus for the typical pulse parameters and

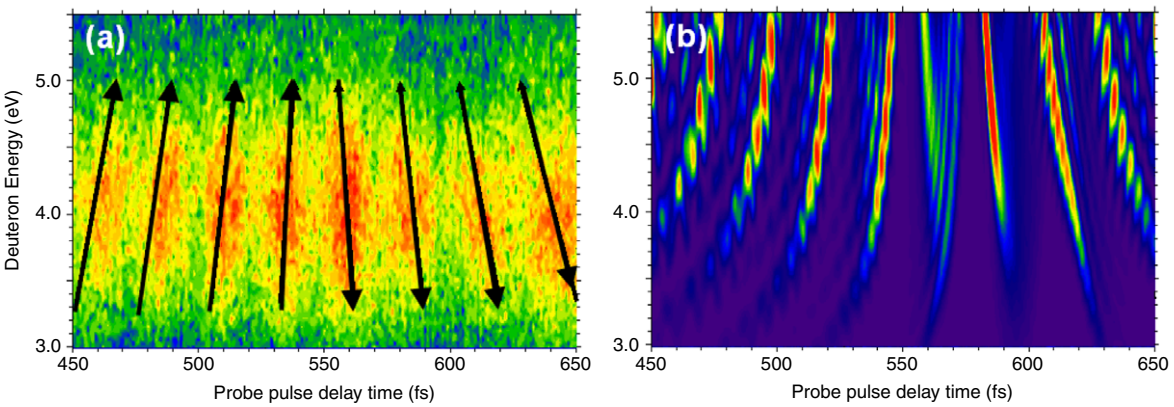

Fig. 12. (a) Vibrational revival structure from the Coulomb explosion of D_2^+ on a linear energy scale. The arrows highlight the direction of wavepacket motion in time. Note these arrows were first fitted to the simulation plot in (b) before being overlaid on (a). (b) For qualitative comparison, a simple direct projection of the wavepacket simulation (Fig. 8 in the revival region) onto the Coulomb potential. This simple projection corresponds to the internuclear range $R = 2.5 \rightarrow 4.5$ au. Both colourscales run from blue to green to yellow to red, with red indicating the highest values. It is useful to note that more complete models of CE have been considered elsewhere, see text for details.

experimental techniques discussed here, it has been important to consider the PD channel in some detail. Since PD is enhanced at specific R values (i.e. near the outer turning point of the wavepacket motion) it provides sensitive information on the molecular vibrational motion.

However, for higher pulse intensities the CE channel will become much more prevalent and provide an insight to the R dependence of the wavepacket tracked through the energetics of the molecular break-up [70]. For high enough probe intensities the CE channel can, in principle, map the wavepacket position across the entire width of the potential well. Here the corresponding appearance energy of the fragments would reflect the internuclear separation at the point at which the wavepacket is lifted onto the CE curve. This energy is inversely proportional to R according to Coulomb's law.

Therefore, one very simple way to consider the basic physics behind the CE channel is as an instantaneous projection of the bound wavepacket onto the Coulomb potential ($\propto 1/R$), occurring around the peak of the probe pulse. The appearance energy (per deuteron) from the Coulomb exploded wavepacket can be easily calculated, by applying this to the wavepacket simulation in Fig. 8. For qualitative comparison with experiment, this has been carried out for probe delay times of 450–650 fs (the revival region) and plotted in Fig. 12(b). The experimental data from Fig. 6 has been expanded in the pertinent region and plotted on a linear scale for appropriate comparison in Fig. 12(a). The colourmaps use similar colour schemes, in order to highlight the important features. Around the revival region, the wavepacket at larger R (*cf.* Fig. 8) will clearly provide the lowest energy release upon CE and at smaller R, the energy release will increase compared to this. The diagonal stripes in Fig. 12 thus correspond to clear localised motion of the wavepacket moving inwards in R (at $<$550 fs) followed by stripes for the wavepacket moving outwards in R.

These stripes can be compared to the experimental data via the eye-guiding arrows on Fig. 12(a). These arrows were initially obtained by fitting to the diagonal stripe structure predicted in (b) and were then overlaid on the energy spectra in (a). The general pattern is extremely consistent, showing that the CE channel provides a signature of the R dependent motion, but the energetics stop short of imaging the wavepacket across the full potential well, due to a limitation from the pulse intensities.

Elsewhere, similar methods have been used to consider the R dependence of wavepacket motion in H_2^+, where a molecular ADK formula was folded into the Coulomb projection and the intensity dependence taken into account [71]. Moreover, with higher pulse intensities the R dependence of the D_2^+ wavepacket has been elucidated with excellent resolution across a larger range of R values [70] where the experimental energy spectrum has been converted to a map of the inferred internuclear separation as a function of pump-probe delay time. It is important to stress that any such wavepacket projection onto the Coulomb curve is a simple technique that is useful for qualitative analysis, but generally will not consider a full quantum treatment of states involved, competing channels or pulse evolution.

More detailed theoretical models have been developed for treating the Coulomb explosion channel [86–88] and for considering the CE imaging techniques in pump-probe wavepacket studies. Most notably, there have been some extremely innovative theoretical studies of the Coulomb explosion imaging technique for extracting spatiotemporal mapping of wavepacket motion towards 'complete characterisation of molecular dynamics' [76].[13] A number of these recent studies are concerned with not only imaging the R dependence of wavepacket motion but also obtaining frequency and energy resolution of the vibrational wavepacket components [75,76,90]. These periodic components are the vibrational beats and can be sought directly from the experimental data.

[13] An extremely attractive extension to the work reported here is to map the wavepacket (in R) with even higher resolution, using an attosecond pulse to induce Coloumb explosion imaging, as proposed in [89]. This should be achievable in the near future.

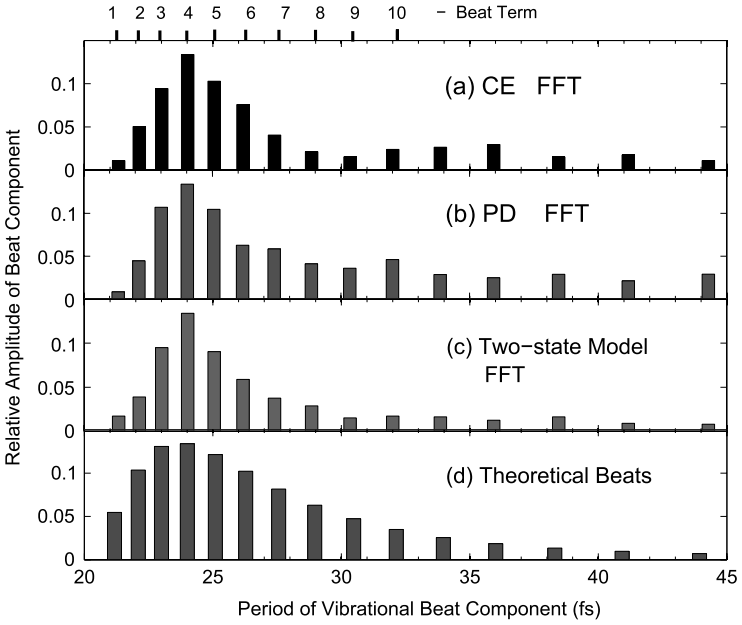

Fig. 13. Vibrational beat frequencies present in wavepacket motion. For comparison with vibrational timescales, the periods ($T_{v',v} = (2\pi/\omega_{v',v})$) of the components are given. The data in plots (a)–(c) were extracted by fast Fourier transform (FFT) analysis. (a) and (b) are FFTs of the CE and PD experimental yields in Fig. 7. The latter can be directly compared to (c), the FFT of the simulated PD yield in Fig. 10. Theoretical beats ($\omega_{v',v}$) for the wavepacket are shown in (d), with associated amplitudes given by $|a_v a^*_{v'}|$. These are the beats for $v' - v = 1$. With reference to (d), the 'Beat Term' positions are also labelled at the top of the figure. Term 1 is for $\omega_{1,0}$, term 4 is for $\omega_{4,3}$ etc ….

9. Fourier transform analysis: Vibrational beats

As is clear from consideration of Eq. (4), the temporal motion of the vibrational wavepacket is dictated by the beat frequencies $\omega_{v',v}$ and the relative amplitudes of the vibrational states. The imaging channels then retrieve information regarding this motion on sub-vibrational timescales. It follows that these periodic contributions to the molecular motion should, in principle, be obtainable from the experimental data by means of Fourier transform analysis [24,67,70,76]. To demonstrate this, values returned from the fast Fourier transform (FFT) of the CE and PD signals from Fig. 7 are displayed in Fig. 13(a) and (b) respectively. The FFT of the two-state PD simulation in Fig. 9(b) is also displayed in Fig. 13(c). The timescale for these frequency components corresponds to the $\omega_{v',v}$ values for $v' - v = 1$ and thus in the context of the vibrational dynamics, the plots in Fig. 13 have been shown on a femtosecond timescale (rather than a frequency axis). For comparison with the wavepacket motion, the theoretical wavepacket beats shown in Fig. 13, are for the periods $(2\pi/\omega_{v',v})$ of the beat frequencies used in Eq. (4) to model the vibrational motion of D_2^+.

In general, the Fourier transform of the cosine function $k.cos(\omega_{v',v}t)$ will return $\frac{k}{2}[\delta(\omega - \omega_{v',v}) + \delta(\omega + \omega_{v',v})]$, i.e. Dirac delta functions at frequencies $\pm\omega_{v',v}$ with the integral of the spikes given by half of the original waveform peak. It is convenient to plot only the positive solutions here. Therefore, as can be seen from Eq. (4), the FFT amplitudes for each component of wavepacket motion should scale proportionally to the $|a_v a^*_{v'}|$ values. For convenience the beats in Fig. 13(d) are plotted against the $|a_v a^*_{v'}|$ amplitudes calculated in Section 5 and plots (a)–(c) have been normalised to the same scale.

The labelled 'beat terms' in the figure are the vibrational beats, where term i is the beat between level i and $i - 1$. That is, term $1 \Rightarrow$ beat frequency $\omega_{1,0}$, term $2 \Rightarrow \omega_{2,1}$ and so on. These beats and the magnitudes of their associated amplitudes, $|a_v a^*_{v'}|$ (calculated in Section 5), are listed in Table 1. It should be noted that the vibrational beats have only been experimentally observed for $v' - v = 1$, i.e. neighbouring vibrational states. Beats contributing to the motion also occur for $v' - v = 2, 3$ etc … on timescales of approximately $\frac{1}{2}, \frac{1}{3}$ … of the 1st order beats respectively.[14] These frequencies are also displayed in Table 1 but are typically not observed in experiment due to the short timescales involved. However for shorter pulse durations these higher order vibrational beats should become observable in future.

Nonetheless, the agreement between experiment and theory is quite striking. The same general trend can be observed in the amplitudes and the temporal agreement of the beats is excellent. However, it is noticeable that the contributions $|a_0 a^*_1|$ and $|a_1 a^*_2|$ (beat terms 1 and 2) are much less significant in the CE and PD FFT than in the wavepacket theory in Fig. 13(d). This is due to the nature of the imaging processes, which cannot easily access the energetically low-lying vibrational levels

[14] Due to the anharmonicity of the potential the energy level spacings are not equidistant and thus the beat frequencies are not at exact multiples of level spacings.

Table 1
Periods of the vibrational beats in D_2^+ (given in femtoseconds). These have been calculated from energy levels obtained using the finite difference technique described in Section 5. The beats $\omega_{v',v}$ are tabulated for $v'-v = 1$, 2 and 3. The values in parentheses are the relative amplitudes, $|a_v a_{v'}^*|$ of each contribution. i.e. the beat between $v = 1$ and $v = 0$ has a period of 21.2 fs and 0.05 relative amplitude in the wavepacket probability density.

Vibrational level v'	Period of Beat Frequency $\omega_{v',v}$		
	Beat with $v'-1$	Beat with $v'-2$	Beat with $v'-3$
1	21.2 (0.05)		
2	22.1 (0.10)	10.8 (0.07)	
3	23.0 (0.13)	11.3 (0.11)	7.4 (0.13)
4	24.0 (0.13)	12.3 (0.13)	7.7 (0.13)
5	25.1 (0.12)	12.8 (0.12)	8.0 (0.12)
6	26.3 (0.10)	13.5 (0.11)	8.4 (0.10)
7	27.6 (0.08)	14.1 (0.09)	8.8 (0.08)
8	29.0 (0.06)	14.9 (0.07)	9.2 (0.06)
9	30.5 (0.05)	15.6 (0.05)	9.7 (0.05)

at these pulse intensities. Thus the PD and CE channels, as with many imaging techniques, do not provide a direct extraction of wavepacket properties but rather, the information is inherently modulated by the dynamics of the allowed fragmentation pathways. This can also be noticed in the higher lying vibrational states (longer timescales) where the CE and PD processes show a relative enhancement in the yield. This is because the higher lying states in the anharmonic $1s\sigma_g$ are energetically more accessible, and indeed close to resonance with the PD process. In fact it is likely that these states are completely depleted by the CE and PD and thus another convention for the relative normalisation of the beats in Fig. 13 could be to use these states to normalise to the theoretical distribution.

For the case of PD imaging, comparison can be made with the FFT of the two-state quantum PD simulation, shown in Fig. 13(c). The shape of the distribution is extremely similar, especially over the first five beat terms and the decreased probability of imaging the low lying levels is also observed in the numerical model. However, at higher levels the experimental signal is again enhanced with respect to the two-state PD simulation. The levels contributing to these beats are energetically close to the resonant 1ω coupling to $2p\sigma_u$ (the so-called '1 photon crossing' at $v = 13$) and this can occur at much lower intensities than the PD of the lower lying levels. The relative enhancement (at high vibrational levels) of the FFT of the experimental PD process may be due to focal volume effects in the experiment, where a large volume of the gas target may experience these low intensities due to the spatial properties of the diffraction limited focus. This is not accounted for in the two-state model. However, the FFT technique provides a second detailed comparison of the two-state model and PD experiment, with convincing agreement.

For the CE imaging, the agreement with the theoretical beats in Fig. 13 is also quite useful qualitatively, but again the nature of the imaging process must be considered before a detailed comparison can be made. Both the R dependence of the CE ionisation and competing PD channel will affect this comparison. For spatiotemporal imaging [70] via the CE channel, the R dependence of the wavepacket can actually be experimentally extracted and it is thus possible to take an FFT in frequency across different R values (not shown here). This innovative technique returns not only the beat frequencies (and thus energy spacings) but also the spatial information about the shape of the $1s\sigma_g$ well. Thus the techniques and principles described here can be extended [75,76,90], for optimum conditions (pulses of <7 fs), to give a full characterisation of molecular structure in both time and space.

The FFT technique has proven to be an excellent method for extracting further information about the nature of the vibrational wavepacket. It serves to retrieve the vibrational beats, in excellent temporal agreement with theory, and provide a good estimation of their relative amplitudes. This is not a detailed method for establishing vibrational distributions created by the pump pulse [63] but is a time-resolved tool for measuring the coherent beats in the wavepacket, by probing on a sub-vibrational timescale. Having extracted detailed characterisation of the vibrational dynamics of the system, the FFT results for longer timescales will now be investigated, and shown to illuminate rotational effects in the molecular motion.

10. Fourier transform analysis: Rotational beats

In the pump-probe experiments for studying bound wavepacket motion, the FFT analysis does not only reveal the aforementioned vibrational beat components, but also identifies periodic contributions on much longer timescales [24,42,70]. These are shown in Fig. 14(c) where the FFT of the CE channel returns rotational beat structures, with frequencies given in THz. These beats can be extracted from experiments using the same configuration as described in Section 5. The beats shown in Fig. 14(a) and (b) were extracted via FFT of a quantum simulation of the rotational motion of D_2 and D_2^+ respectively. It is instructive to introduce the rotational wavepackets discussion through simulations at this point, as they provide useful timing and amplitude comparisons, although a discussion of the simulation technique will not be provided until Section 11.

Similar to the vibrational case, a rotational wavepacket can be initiated impulsively in intense laser fields and is created in a coherent superposition of states, which may exhibit field-free evolution after the pulse has elapsed. Impulsive alignment can occur if the pulse is sufficiently short compared to the rotational timescale of the molecule [91,92]; it can be used to

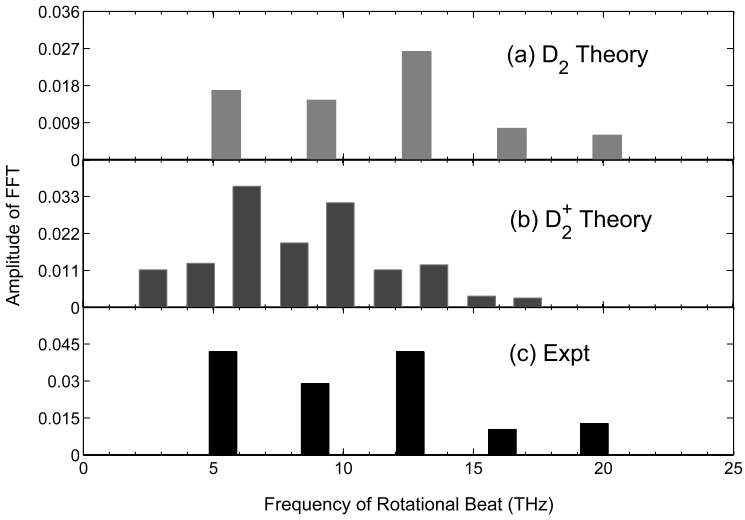

Fig. 14. Rotational beat frequencies present in wavepacket motion. (a) and (b): FFT of quantum simulations of impulsively aligned D_2 and D_2^+ respectively. The calculations of rotational motion were made for a 12 fs, 2×10^{14} W cm^{-2} aligning pulse, see Section 11 for details. (c) FFT of CE experimental yield for 12 fs pump-probe experiment on D_2 target.

provide field-free aligned molecular ensembles and has previously been demonstrated in larger molecules which move on much slower timescales (e.g. see [91] and references therein). In this way, delicate control can be enforced over the rotational dynamics and bond alignment (for example, see [91–96].

Since rotational timescales in the D_2/D_2^+ systems are much longer than the vibrational timescales, pulses of durations <15 fs may be used to initiate such impulsively aligned rotational wavepacket motion [26,27,42]. This may be expressed in terms of a basis set of rotational *(J)* states, in a similar form to Eq. (3) but with an angular dependence introduced into the eigenstate basis set (e.g. using spherical harmonics, see [27,92] for more detail). The evolution of the rotational wavepacket is dictated by beat frequencies between level J and some level J'. This again is highly analogous to the vibrational dynamics. Within the rigid rotor approximation, the energy of the Jth rotational state is given by $E_J = BJ(J+1)$, where B is the rotational constant. For a homonuclear diatomic molecule, the only allowed Raman transitions to excite the wavepacket are for $\Delta J = 0, \pm 2$, and since beats between 'neighbouring' states are expected to dominate [97], the predicted beats are given by

$$\omega_{J+2,J} = \frac{E_{J+2} - E_J}{\hbar} = \frac{B}{\hbar}\{(J+2)(J+3) - J(J+1)\} = (4J+6)\frac{B}{\hbar}. \tag{10}$$

The substitution $\omega_1 = \frac{2B}{\hbar}$ can be made [97] to alternatively write $\omega_{J+2,J} = \{2J+3\}\omega_1$ and thus the period of each beat can be written as a fraction of the fundamental period of $J = 1$ (where $T_1 = \frac{\pi\hbar}{B}$) such that

$$T_{J+2,J} = \frac{2\pi}{(2J+3)\omega_1} = \frac{1}{2J+3}T_1. \tag{11}$$

Since the periods of the beats are given by fractions of T_1 ($\frac{1}{3}$, $\frac{1}{5}$, $\frac{1}{7}$ ...) these components will all be in phase again after one full period of T_1, having executed 3, 5, 7 ... oscillations. Therefore any *rotational revival* will be expected to occur at T_1 after the initial alignment.

Now if B is given in wavenumbers, the fundamental period can be denoted by $T_1 = (2Bc)^{-1}$ and thus the beat frequencies for rotational motion in D_2 and D_2^+ can be simply calculated using B values of 30.44 cm^{-1} and 15.02 cm^{-1} respectively [98], giving the values in Table 2. These values provide a useful comparison to the experimentally deduced beats shown in Fig. 14(c), and are also consistent with the FFTs of the quantum alignment simulations, plotted in Fig. 14(a) and (b).

Upon comparison of the experimental FFT plots in Fig. 14 with the simulation FFTs in Fig. 14 and the values in Table 2, it is fascinating to observe that the *periodic* rotational effects observed in the experiment are not actually characteristic of the D_2^+ ion. Rather, it appears that they are signatures of the D_2 neutral. This is contrary to preliminary assertions made elsewhere [70], where these rotational features were initially attributed to D_2^+. However, the results shown here clearly demonstrate correlation between experiment and the characteristics of D_2 rotations, not only in the timing of the beats but also in the relative amplitudes of the beat contributions to the wavepacket motion. Although there may be some rotational effect due to the D_2^+ ion, it is not clearly seen in the periodic contributions to the experimental signal and this will be discussed in due course.

Table 2
Rotational Beats of D_2 and D_2^+. For convenient reference, the beats are given in THz and their corresponding periods ($2\pi/\omega$) are in femtoseconds. These beats are evaluated from Eq. (10) and are consistent with those displayed in Fig. 14 from quantum simulations.

Beat $J \rightarrow J+2$	D_2		D_2^+	
	Frequency (THz)	Period (fs)	Frequency (THz)	Period (fs)
$0 \rightarrow 2$	5.48	182.61	2.65	377.16
$1 \rightarrow 3$	9.13	109.57	4.42	226.30
$2 \rightarrow 4$	12.78	78.26	6.19	161.64
$3 \rightarrow 5$	16.43	60.87	7.95	125.72
$4 \rightarrow 6$	20.08	49.80	9.72	102.86
$5 \rightarrow 7$	23.73	42.14	11.49	87.04

As stated, the pump pulse wavepacket excitation/creation occurs in steps of $\Delta J = \pm 2$, from the initial rotational states. The amplitudes of the rotational components in the final wavepacket are therefore clearly influenced by the initial rotational distribution. Thermal averaging is accounted for in the model used to predict the amplitudes in Fig. 14(a) and (b).

Another property of the system influencing the rotational distribution is the effect of nuclear spin permutations. The nuclei in D_2 are bosons, and thus the total wavefunction $\Psi = \Psi_{elec}\Psi_{vib}\Psi_{rot}\Psi_{nucspin}$ must be symmetric upon exchange of particles. The initial electronic state and the initial $v = 0$ vibrational state in D_2 are both symmetric. The ortho nuclear spin state (symmetric) must then correspond to a J_{even} (symmetric) rotational state. Conversely, the para spin state (anti-symmetric) corresponds to J_{odd}. In general for homonuclear diatomic molecules with nuclear spin I, there are $(2I+1)(I+1)$ symmetric and $(2I+1)I$ antisymmetric nuclear spin wavefunctions. Thus the ratio of (ortho:para) states is $(I+1:I)$ and for D_2 ($I = 1$) this infers a ratio of 2:1 for $J_{even} : J_{odd}$. This feature is accounted for in the theoretical model and is clearly reflected in Fig. 14 where the beats $J = 0 \rightarrow 2, 2 \rightarrow 4$ are much more dominant than the $J = 1 \rightarrow 3$ and $3 \rightarrow 5$ components.

11. D_2 rotational wavepacket motion: An underlying effect in vibrational studies of D_2^+

From both the timing and relative amplitudes of the beats, the results in Section 10 imply that the rotational signatures in such pump-probe studies are characteristic of the D_2 neutral. Observations of such rotational motion are not restricted solely to FFT analysis, as closer inspection of Fig. 7 reveals underlying modulations on longer timescales than the vibrational dynamics. A dip and peak structure is observed around 270 fs, and the vibrational revival structure itself actually appears to sit on a peak-dip structure. These modulations are consistent with the field free motion of an impulsively aligned D_2 target [26,27], and the signatures are consistent with several pump-probe studies of D_2^+ vibrational wavepackets [24,42,70]. Does this then imply that in such experiments the D_2^+ molecule is rotating with D_2 neutral characteristics? The results shown in Fig. 15 will help to address this confusing issue.

Displayed in Fig. 15(d) and (e) are numerical simulations of rotational wavepacket motion for impulsive alignment of D_2 and D_2^+ respectively. These systems were modelled by solving the time-dependent Schrödinger equation for the respective molecules. This procedure has been described in detail elsewhere [92] and includes thermal averaging over the rotational states in the room-temperature ensemble. The approach enables the expectation value $\langle cos^2\theta \rangle$ to be calculated, where θ is the angle made with the initial alignment axis. By common convention, this quantity is used as a measure of the degree of wavepacket alignment where $\langle cos^2\theta \rangle = \frac{1}{3}$ corresponds to an isotropic distribution.[15] For the temporally evolving rotational wavepacket, this property can be plotted as a function of pulse delay time (see Fig. 15(d) and (e)). For convenient comparison to the experiment, the $\langle cos^2\theta \rangle$ axis runs in the reverse direction, as the experiment probes 'anti-alignment' with respect to the aligning pulse (i.e. the pump pulse is perpendicular to the detection axis and the probe pulse parallel). The FFT of the temporal evolution model then gives the relative amplitudes of the beats considered earlier in Fig. 14(a) and (b).

These wavepacket models can be compared to the plots in Fig. 15(a)–(c), which are for a pump-probe experiment carried out using the same experimental technique as in Section 5, where the pump pulse is perpendicular to the detection axis and the probe is parallel. The PD and low energy CE yields may be compared with those in Fig. 7, displaying established vibrational wavepacket dynamics. However, here a significant yield of high energy CE (>5 eV per deuteron) is also observed, and the integrated yield of this high energy band is plotted in Fig. 15(c). The integrated yield has, noticeably, no vibrational characteristics present! This is because the majority of the data in this high energy band is displaying CE imaging of the D_2 molecule where the fragments are at high energy due to the small internuclear separations at which CE occurs. This becomes clear when one considers the electronic surfaces in Fig. 3, where the D_2 bond in $v = 0$ exists at smaller R than the D_2^+ ion. This direct CE imaging technique is therefore used to image an impulsively created rotating wavepacket, and the small extraction aperture of the system acts to probe <2 degrees angular acceptance at these high energies of >5 eV.

Therefore, in this particular experiment, rotational wavepacket motion is being probed orthogonally to the initial alignment axis, where a peak is effectively a measure of anti-alignment and a dip infers orientation along the initial alignment

[15] Using spherical polar coordinates, θ is the polar angle and for an isotropic distribution symmetry is assumed about the azimuthal angle ϕ, and thus $\langle cos^2\theta \rangle = \int cos^2\theta d\Omega / \int d\Omega = \frac{1}{2}\int_0^\pi cos^2\theta sin\theta d\theta = \frac{1}{3}$.

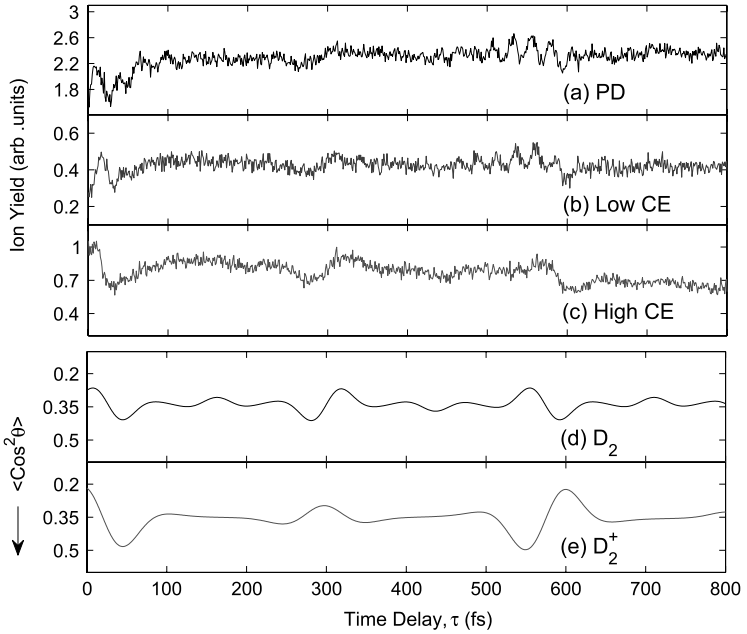

Fig. 15. Vibrational and rotational wavepacket signatures in 12 fs pump-probe studies on a D_2 target. The vibrational dynamics from experimental studies, in plots (a) and (b), sit on a background modulation due to rotational effects. By comparison with simulations of rotational wavepacket alignment in (d) D_2 and (e) D_2^+ (measured by $\langle cos^2\theta \rangle$) for a 12 fs and 2×10^{14} W cm^{-2} pulse, it can be seen that the rotational effects are characteristic of the D_2 molecule, in keeping with Fig. 14. The $\langle cos^2\theta \rangle$ axis is plotted in reverse direction for convenient comparison to the experiment, which measures wavepacket orientation perpendicular to the alignment axis, by probing orthogonal to pump direction. (c) The integral of the high energy products (>5 eV) arises solely from CE of the D_2 system (at small R) and displays excellent correlation with D_2 rotational theory. This implies that the pump pulse can create *either* a vibrational wavepacket in D_2^+ *or* a rotational wavepacket in D_2, with the probe imaging both wavepackets via PD or CE.

axis. The peak followed by a dip in the 550–600 fs region in Fig. 15(c) is thus a retrieval of the initial alignment conditions and this is the *rotational revival*, due to the re-phasing of the rotational beats.

Comparison of the wavepacket theory and the experimental yield serves to further confirm the periodic D_2 signatures, rather than D_2^+. The revival should occur at $(2Bc)^{-1}$ and for D_2 this is ∼550 fs. Since the revival time interval is the time taken to return to initial conditions, this can be measured as the centre of the peak-dip near $t = 0$ to the centre of the peak-dip at the revival and this time is clearly consistent with the $(2Bc)^{-1}$ value. At around 270–300 fs in both experiment and D_2 theory there is another revival-like structure for the rotational wavepacket. This structure implies that the molecule is first orientated along the alignment axis (dip in the signal) and then perpendicular to the alignment axis (peak in the signal). The degree of alignment is of the same magnitude as the revival, but it is not strictly a full retrieval of initial conditions in the temporal progression. Occurring after $\frac{1}{2}(2Bc)^{-1}$, it is the *half* revival of the rotational wavepacket. Other fractional revivals can be seen as smaller modulations in the $\langle cos^2\theta \rangle$ value, at $\frac{1}{4}$ and $\frac{3}{4}$ multiples of the revival time.

Now having fully characterised the presence of D_2 rotational motion (and the lack thereof of periodic coherent D_2^+ rotations), Fig. 15 can be used to address what is a complex aspect of such pump-probe experiments. From the analysis of the data presented in this report, it appears that the pump pulse can create *either* a coherent rotational wavepacket in D_2 *or* a coherent bound vibrational wavepacket in D_2^+. The probe pulse can access either wavepacket by CE or by PD. For the vibrating D_2^+ wavepacket, direct PD or CE images the vibrating D_2^+ ion. For the rotating wavepacket, CE and PD occur after the intermediate stage of D_2^+ (or by direct recollision induced ionisation of D_2 to give CE products).

So, the experimental yield that is observed appears to be effectively due to two separate experimental ensembles where the separate vibrational studies of D_2^+ [24,70] and rotational studies of D_2 [26,27] make use of the same imaging channels (referred to as PD and CE in this article). It is therefore difficult to experimentally isolate the D_2^+ vibrating wavepacket from the D_2 rotational wavepacket imaging. One possibility is to make some background subtraction of the purely rotational contribution, as found in the higher energy CE fragments, from the lower energy CE and PD yields. This has been done elsewhere [24] and provides a useful approximation to extracting isolated signatures of D_2^+ vibrations from the data. However, this method does not strictly direct the dynamics or isolate the wavepacket motion occurring in the experiment but rather selectively extracts desired signatures from the data. Nonetheless, in the experimental work reported to date the rotational background has been much smoother and slowly varying than the vibrational data and thus has not significantly clouded the elucidation of the vibrational dynamics [24,70,71].

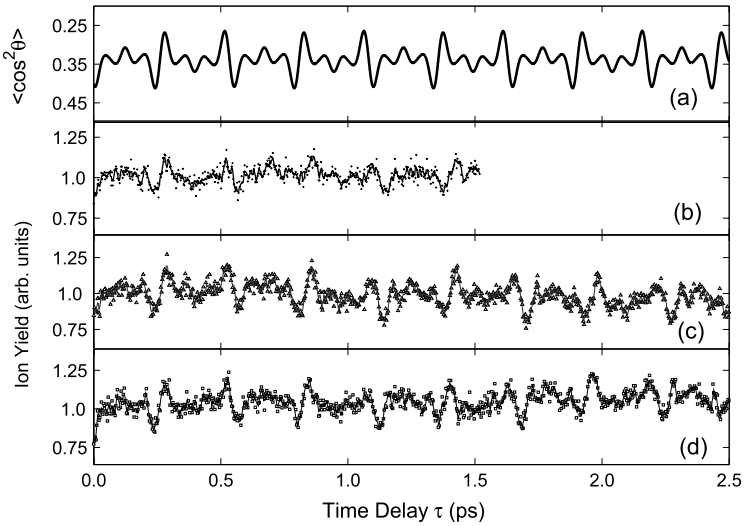

Fig. 16. Rotational wavepacket motion in D_2 over a picosecond (ps) time range. (a) Simulated wavepacket alignment for a 12 fs pump pulse. Experimental observations for aligning pulses of 12 fs, 40 fs and 100 fs durations are shown in (b), (c) and (d) respectively. The probe pulse was 12 fs in each case. The data points were taken in steps of 3 fs and the 3 point average is plotted (solid line in each plot) to guide the eye, displaying good correlation with the simulated progression of wavepacket motion.

It is important to stress that this is not to say there are *no* rotational effects in the D_2^+ ion, rather that there are no *periodic retrievals* of alignment. Indeed, one may notice that the PD yield in Fig. 15 appears to be particularly dipped around the first 50 fs, more so than at any later times where D_2 alignment is retrieved. This effect may be due to *transient* alignment of D_2^+ [42], where the aligning pulse induces an initial rotational motion but there is no consequent revival due to the broad distribution of active vibrational states, each with their own rotational constants. That is, the D_2^+ ion is created in such a large range of vibrational states, each with an associated range of rotational states, that the range of ro-vibrational contributions may in fact average out to give an effectively isotropic distribution. Thus rotational motion can occur in the D_2^+ ion, but it is not coherent and thus no periodic signatures are retrieved. This is consistent with results seen in [24,42].

Also, the rotating D_2 that has been observed appears to vibrate incoherently, although it should be noted that coherent vibrational motion can be initiated in D_2 if shorter pulses [99,100] are used.

It has been shown in this section that the rotational wavepacket dynamics in D_2 *can* be isolated from vibrational signatures by observing high energy Coulomb explosion fragments and this has been shown to match well with the predicted wavepacket dynamics. This can be further studied by varying the duration of the pump pulse and keeping the probe fixed to image the rotational wavepacket structure, providing results as shown in Fig. 16. The pulse duration was stretched using the technique discussed in Section 7, resulting in lower peak intensities for longer pulse durations. In the figure, a three point averaging has been applied to display the solid lines on each plot of experimental data.

It is very interesting to observe that the initiation of coherent rotational wavepacket motion in D_2, can be achieved with up to 100 fs pulses. This may be a little surprising given that such rotational wavepacket motion has only been resolved in detail relatively recently,and this was achieved with <15 fs pulses [26,27,42]. However it follows that the limitation in achieving these observations previously was actually in the *probe* pulse duration required to take an ultrafast snapshot of the rotating structure.

From the data shown here, there has been a clear indication of rotational wavepacket structure and the underlying dynamics are now well understood. As the temporal evolution of wavepacket dynamics has been the main focus, the degree of alignment has not been directly extracted from the experimental data but the comparison with the $\langle cos^2\theta \rangle$ plots shows excellent agreement. The results shown here are consistent with a recent study of D_2 alignment using 12 fs pulses [24] and in two other recent studies 10 fs [26] and 8 fs [42] aligning pulses have been used. In [24,26] the pulse peak intensities were 2×10^{14} W cm^{-2} and in [42] the intensity was 3×10^{14} W cm^{-2}. The latter two studies have directly sought a measure of the $\langle cos^2\theta \rangle$ parameter, returning maximum values of $\sim$0.41 and 0.36 respectively. This is consistent with the results in Fig. 16, where the longer pulse duration of 12 fs is simulated to provide a maximal alignment upwards of 0.4. Therefore, the 8 fs pulse appears to provide less impulsive alignment as the field is not on for long enough, and the longer pulse durations provide slightly improved alignment. However it is important to stress that the maximum degree of alignment is still *relatively small* compared to larger, more polarisable molecules where impulsive alignment provides a very clear scheme for ensemble alignment (for example see [95]). Nonetheless, it is a significant achievement that the coherent rotational motion of this fundamental fast molecule has now been induced and imaged in a time-resolved experiment; owing especially to the short *probe* pulse duration.

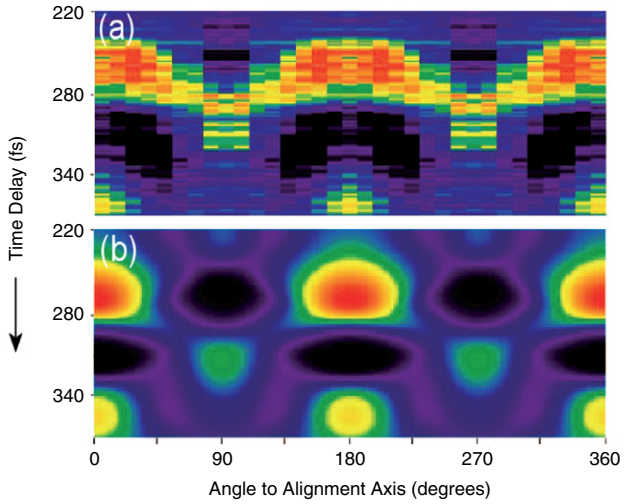

Fig. 17. 'Quantum carpet' of an impulsively aligned D_2 rotational wavepacket. (a) Experimental observation. The angle between the pump and probe pulses was varied to selectively image different angular sections of the wavepacket. (b) Quantum model of temporally evolving angular dependence of wavepacket with respect to the 12 fs alignment pulse. In (a) and (b) the colourscale represents the yield and probability density, thus providing good comparison between experiment and theory. Low yield/probability is represented by black, to purple and then the values increase across the visible spectrum to the higher yields being shown as red.

12. Angular dependence of D_2 rotational wavepackets

Even though the degree of molecular alignment may be small, the structures of alignment and rotational revivals can be clearly resolved in the experiments. In the data shown in this article, the wavepacket probing was carried out along the TOFMS detection axis, thus imaging only a slice of a few degrees of the molecular ensemble.

The full angular dependence of the impulsively induced rotational wavepacket can be measured by manipulating the relative orientation of pump and probe pulses, availing of the small angular acceptance of the TOFMS. By keeping the probe pulse polarisation in the plane of the detector, the resulting high energy CE fragments will provide imaging of the wavepacket. The pump pulse polarisation may then be rotated to some angle θ with respect to the probe axis. Thus the probe will be imaging the wavepacket at an angle θ to the initial alignment axis. By rotating θ through a full range of values a full picture of the angular dependence of the wavepacket can be retrieved.

The results from an experimental implementation of this technique are shown in Fig. 17 and compared with a theoretical distribution, the so-called 'quantum carpet'. This technique has been recently demonstrated [27] and provides excellent characterisation of the rotational wavepacket in D_2. The particular example shown in Fig. 17 is for a 12 fs aligning pulse and is shown around the region of the first half revival. The vertical cut through the colourmap at $\theta = 90$ degrees is equivalent to the high energy CE yield in Fig. 15 between 220 and 340 fs. The colourscale runs from the low yield/probability being represented by black/purple with values increasing across the visible spectrum to the higher yields being shown as red. Thus at 270 fs there is strong probability of orientation along the initial alignment direction and low probability of alignment orthogonal to pump pulse orientation. At around 310 fs this distribution has then shifted to now give an enhanced orientation orthogonal to the alignment direction (90 degrees) and a suppressed probability of alignment at 0 degrees. The repetition of the data through 180 degrees to 360 degrees provides a useful eye guide for comparison to theory, providing excellent agreement and further characterising the fast rotational wavepacket motion.

13. Vibrational excitation of D_2

In the aforementioned recent pump-probe studies of D_2 [26,27,42], rotational wavepacket motion has been identified but there has been no indication of coherent vibrations in D_2. There is, however, a recent exception to this where signatures of vibrational motion in the neutral molecule have been observed [99].

First, it is instructive to note that at room temperature, the D_2 molecule is in its ground vibrational state $v = 0$, and in the absence of any external interaction there is clearly no coherent vibrational motion. We recall that in order to induce a dynamic coherent wavepacket, it is desirable to create a superposition of states on a sub-vibrational timescale. For example, in D_2^+ it has already been seen that vibrational wavepacket excitation can be initiated via ultrafast tunnel ionisation where the projection of D_2 ($v = 0$) onto the $1s\sigma_g D_2^+$ surface results in a broad superposition of vibrational states. It is the relative evolution of the phases of these eigenstates that leads to the motion of the wavepacket and indeed the de-phasing and revival dynamics that have been discussed in this report. In D_2 however, it is not initially clear as to how one may initiate a coherent wavepacket in an analogous manner and, as will now be discussed, an alternative mechanism (to ionisation) may occur to excite the wavepacket.

In a pump-probe experiment reported by Ergler et al. [99], D_2^+ ions and D^+ ions (from the $D + D^+$ dissociation channel) were detected as a function of pump-probe delay across a time range in excess of 1 ps, using two 7 fs pulses with peak intensities at 4×10^{14} W cm^{-2}. Across the full time range, the D_2^+ yield was found to continually oscillate with a period of 11.10 fs and the yield of D^+ ions was conversely modulated with the same periodicity. This period is fascinatingly consistent with the spectroscopic frequency difference between $v = 0$ and $v = 1$ in D_2, which corresponds to a timescale of 11.14 fs [101].

Recalling the discussion in Section 9, it therefore appears that the oscillation in the experimental data is due to a 'beating' between these two eigenstates. Indeed, if one were to explicitly evaluate Eq. (4) (page 25) for a superposition of just two eigenstates, it is clear that a single frequency will govern the subsequent wavepacket motion, given by the frequency difference of the two states. So from this experimental evidence, it appears that a dynamic wavepacket can be induced through vibrational excitation of D_2, into a superposition of $v = 0$ and $v = 1$, but how does this occur?

A recent theoretical study led to a proposed mechanism for this, through 'lochfraß' [100] (the German word for eating a hole or pitting corrosion). In this innovative article, the authors assert that wavepacket formation in the neutral molecule can occur due to a 'pronounced dependence of the strong-field ionisation rate on the internuclear distance'. Basically, for the pump pulse interaction under appropriate conditions the probability of ionisation to D_2^+ increases towards larger R values and this interaction acts to modulate the D_2 wavepacket, effectively shifting the remaining population towards smaller R. After the ultrafast pump pulse interaction, the wavepacket that remains on the ground electronic surface of D_2 is no longer exclusively in the $v = 0$ eigenstate and now resides in a coherent superposition of $v = 0$ and 1. Thus a vibrational wavepacket will subsequently execute oscillations back and forth across the groundstate electronic surface of D_2. The probe pulse interaction then tracks this motion back and forth across the potential, where the yields are modulated with the periodicity of the wavepacket oscillation.

Since the wavepacket oscillates with a single frequency, a viable application for future pump-probe studies in the gas phase would be to use the D_2 oscillation for precision timing. This could be conducted for any pump-probe study in the gas phase, where a small amount of D_2 gas could be mixed in with the target and thus the oscillation in D_2^+ yield would provide a known reference timescale (i.e. an fs 'molecular' clock). Further to this, the lochfraß mechanism also provides a more general scheme for initiating vibrational wavepackets in neutral molecules beyond the hydrogen diatomics (e.g. in hot I_2 molecules [102]).

14. Future outlook

This report has conveyed key aspects of recent pump-probe experiments which have provided time-resolved mapping of molecular wavepacket dynamics in hydrogen molecules, using ultrashort femtosecond laser pulses. These studies have enabled wavepacket motion to be initiated then, following evolution in a field-free environment, to be tracked as a function of time, with results providing rich information about the molecular dynamics.

In the past few years, other strides have been made in studies of these fundamental molecules in intense laser fields. For ionisation and fragmentation events there have been detailed investigations of pathways and energetics for both neutral targets (e.g. [28–31]) and ion beams (e.g. [34–39]). Beyond this, other exciting advances are now being made in short pulse studies of imaging/controlling molecular dynamics.

In recent experiments, the laser-induced electron re-collision process has been utilised as a probe of molecular evolution in the presence of the laser field. A re-colliding electron wavepacket effectively provides a sub-cycle (attosecond) probe that can image H_2^+ (or D_2^+) bond evolution via fragmentation or via high-harmonic generation. The former technique is dubbed the 'molecular clock' scheme and was developed by Niikura et al. [52,53] in the group of Corkum and Villeneuve at the NRC (Ottawa), with a useful complementary discussion given in [103]. The latter technique was pioneered by Baker et al. [55,104] in the group of Marangos and Tisch at the Blackett laboratory, Imperial College (London) and has been allocated the acronym 'PACER', standing for 'probing attosecond dynamics by chirp-encoded re-collision'. A useful review of molecular imaging using re-colliding electrons is given in [105], where tomographic imaging [106,107] of molecular structure is also discussed, as well as the aforementioned re-collision techniques for temporal evolution studies.

These innovative re-collision techniques provide excellent information on molecular evolution, but are naturally restricted to observing dynamics which occur *in the presence* of a strong driving field. A proposed extension to the PACER technique is to first excite the molecule with a pump pulse, allow it to evolve field-free, and then use a probe pulse to generate high-harmonics which provide a measure of wavepacket autocorrelation [108]. This would enable high-harmonic techniques for tracking longer term wavepacket evolution. This is an interesting prospect but will not necessarily retrieve any significant information on wavepacket dynamics that has not already been elucidated in the pump-probe schemes outlined in this report.

An elegant progression from the mapping of wavepacket dynamics reported here, would be to demonstrate coherent ultrafast control over the wavepacket motion. Intense-field induced control over the vibrational superposition has been proposed [84], where theoretical studies have established schemes for non-destructive manipulation of wavepacket amplitudes and phases; therein coherently controlling the wavepacket motion. This is in the spirit of existing coherent control methods (e.g. see [109–111]) but is being carried out at much higher laser intensities and on a previously inaccessible timescale. The superposition may be vibrationally cooled [84] or driven towards tailored distributions such as a single-state population [83] or a two-state superposition [79]. A so-called 'quantum chessboard' has been used to provide an overview

of the range of outcomes for such intense-field control and, in particular, highlights the ability to create either exclusively even or exclusively odd states [66]. Although much consideration has been given to techniques for implementing such state-selective control [82], experimental verification has remained difficult to achieve [113]. It should be noted in this context that control of the nuclear (vibrational) wavepacket has been demonstrated to an extent, through selective dissociation of the molecule [47,69,112].

Perhaps a more notable form of wavepacket control is the ability to guide the electron, where one interesting scheme is to seek localisation of the electron on a chosen nucleus during the molecular break-up. A landmark experiment by Kling et al. [49], in a research collaboration between the groups of Vrakking (Amsterdam) and Krausz (Garching), has provided proof-of-principle evidence for such control and this has stimulated significant theoretical interest [114–117] in optimising the ability to steer the electron localisation. Indeed for studies in hydrogen diatomics, this is a process that should benefit significantly by availing of the nuclear wavepacket properties that have been discussed in this report. This a promising area of study and should see significant advances in the next few years, building on the work reported here.

Such schemes that have been established and fine-tuned in fundamental systems will also find applications in larger molecular targets. Spectral pulse shaping techniques are currently providing experimentalists with an adaptive tool [118,119] for targeting the cleavage of specific chemical bonds (e.g. in amino acids [120]) and shorter pulse durations may even enable ultrafast electron transport processes to be studied [121]. This builds on the existing application of femtosecond lasers in gas-phase chemistry [122] and other pump-probe spectroscopy studies [123]. Such studies in larger molecular systems show particular promise in the context of new laser and X-ray technology and it is in molecules of biological interest that some of the most significant benefits promise to be realised.

Prior to this, it will be of paramount importance to establish fundamental mechanisms by testing out new laser technology on fundamental molecular targets. Moreover the new sources for ultrafast X-ray pulses [124,125] and high-harmonic attosecond pulses [126–129] promise to probe hydrogen diatomics with wavelengths comparable to the nuclear separation and on timescales comparable to the electronic motion. For example, an extremely attractive extension to the work reported here would be to probe the D_2^+ vibrational wavepacket with an attosecond pulse, as proposed in [89], leading to potentially unprecedented resolution in the imaging of the wavepacket. With ongoing advances in laser technology such progress should be realised in the near future. Indeed, the 'ultrafast' progress in this field of research is epitomised by a few articles published during the proof stage of this report. There has been new insight into dissociative double ionisation of D_2 [132], the use of an attosecond pump pulse in D_2^+ wavepacket studies [130] and the application of vibrational wavepacket dynamics in few-cycle pulse studies of electron localisation [133,134].

We fully expect that the hydrogen diatomics will continue to act as a crucial test-bed for formative studies with new laser technology and that they will be subjected to further intensive time-resolved studies using few-cycle CEP-locked IR pulses and XFEL/attosecond pulses. Advances in ultrafast pulse technology promise the next exciting step forward in time-resolved molecular dynamics; imaging and controlling the motion of the electron.

Acknowledgements

The sample experimental data used in this report, to explain the general advances in this area of research, was obtained through experiments carried out by the authors on the Astra Laser at the Central Laser Facility, Rutherford Appleton laboratory, Oxfordshire, England. The authors would like to acknowledge the invaluable contributions to this research from Jarlath McKenna, Raymond King, John Alexander and Jason Greenwood (Queen's University Belfast), Joseph Wood and Elizabeth English (University College London) and Jamie Nemeth (Swansea University).

The authors would also like to acknowledge Domhnall Murphy and Jim McCann (Queen's University Belfast) and Ricardo Torres (Imperial College London) who have made important contributions to the modelling of vibrational and rotational dynamics respectively. Chris Calvert would also like to thank Colin Latimer (Queen's University Belfast) and Ian Walmsley (Oxford) for stimulating and insightful discussions.

Thanks also goes to the staff on the Astra laser at Rutherford Appleton Laboratory; Edmond Turcu, Emma Springate, Chris Froud, Steve Hawkes, Klaus Ertel, Oleg Cheklov, Chris Hooker, Edwin Divall, Andrew Langley and John Collier. The experiments were undertaken with the financial support of the Engineering and Physical Sciences Research Council (UK) and Science and Technology Facilities Council (UK). Chris Calvert acknowledges funding from the Department for Employment and Learning (NI).

References

[1] R.P. Madden, K. Codling, Phys. Rev. Lett. 10 (1963) 516.
[2] For example J.M. Hollas, Modern Spectroscopy, Fourth Edition, John Wiley and Sons, 2005.
[3] P.F. Moulton, J. Opt. Soc. B 3 (1986) 125.
[4] D. Strickland, G. Mourou, Optics. Comm. 56 (1985) 219.
[5] A.H. Zewail, Science 242 (1988) 1645.
[6] A.H. Zewail, J. Phys. Chem. A 104 (2000) 5660.
[7] J.H. Posthumus, Rep. Prog. Phys. 67 (2004) 623.
[8] A. Giusti-Suzor, F.H. Mies, L.F. DiMauro, E. Charron, B. Yang, J. Phys. B: At. Mol. Opt. Phys. 28 (1995) 309.
[9] B. Sheehy, L.F. DiMauro, Annu. Rev. Phys. Chem. 47 (1996) 463.
[10] Th. Ergler, A. Rudenko, B. Feuerstein, R. Moshammer, J. Ullrich, et al. For example, see references [23,40,58,70,71,99].

[11] H. Niikura, F. Légare, K.F Lee, D.M. Villeneuve, P.B. Corkum, et al. For example, see references [25,26,52,53,69,72,84,112].
[12] A.S. Alnaser, I.V. Litvinyuk, I. Ben-Itzhak, C.D. Lin, C.L. Cocke, T. Niederhausen, U. Thumm, For example, see references [42,60,61,74–76,83].
[13] S. Baker, J.P. Marangos, J.W.G. Tisch, et al. For example, see references [55,104].
[14] M.F. Kling, M.J.J. Vrakking, et al. For example, see references [49,50,130].
[15] W.A. Bryan, W.R. Newell, I.D. Williams, J.F. McCann, et al. For example, see references [24,27,47,59,66–68,79,82].
[16] W.C. Wiley, I.H. McLaren, Rev. Sci. Instrum. 26 (1955) 1150.
[17] J. Ullrich, et al., J. Phys. B 30 (1997) 2917.
[18] I.C.E. Turcu, et al. Central Laser Facility (UK) Annual Report 2004–2005 - http://www.clf.rl.ac.uk/reports/2004-2005/pdf/100.pdf.
[19] M. Nisoli, S. De Silvestri, O. Svelto, Appl. Phys. Lett. 68 (1996) 2793.
[20] R. Szipocs, K. Ferencz, C. Spielmann, F. Krausz, Opt. Lett. 19 (3) (1994) 201.
[21] R. Trebino, D.J. Kane, J. Opt. Soc. Amer. A 10 (1993) 1101.
[22] C. Iaconis, I.A. Walmsley, Opt. Lett. 23 (1998) 792.
[23] Th. Ergler, A. Rudenko, B. Feuerstein, K. Zrost, C.D. Schröter, R. Moshammer, J. Ullrich, Phys. Rev. Lett. 95 (2005) 093001.
[24] W.A. Bryan, et al., Phys. Rev. A 76 (2007) 053402.
[25] F. Légare, K.F. Lee, I.V. Litvinyuk, P.W. Dooley, A.D. Bandrauk, D.M. Villeneuve, P.B. Corkum, Phys. Rev. A 72 (2005) 052717.
[26] K.F. Lee, F. Légare, D.M. Villeneuve, P.B. Corkum, J. Phys. B. 39 (2006) 4081.
[27] W.A. Bryan, E.M.L. English, J. McKenna, J. Wood, C.R. Calvert, R. Torres, I.C.E. Turcu, J.L. Collier, I.D. Williams, W.R. Newell, Phys. Rev. A. 76 (2007) 023414.
[28] A. Staudte, et al., Phys. Rev. Lett. 102 (2009) 033004.
[29] B. Manschwetus, T. Nubbemeyer, K. Gorling, G. Steinmeyer, U. Eichmann, H. Rottke, W. Sandner, Phys. Rev. Lett. 102 (2009) 113002.
[30] S. Saugout, E. Charron, C. Cornaggia, Phys. Rev. A 77 (2008) 023404.
[31] A. Staudte, et al., Phys. Rev. Lett. 98 (7) (2007) 073003.
[32] I.D. Williams, et al., J. Phys. B. 33 (2000) 2743.
[33] K. Sandig, H. Figger, T. Hansch, Phys. Rev. Lett. 85 (2000) 4876.
[34] P.A. Orr, I.D. Williams, J.B. Greenwood, I.C.E Turcu, W.A. Bryan, J. Pedregosa-Gutierrez, C.W. Walter, Phys. Rev. Lett. 98 (2007) 163001.
[35] J. McKenna, et al., Phys. Rev. Lett. 100 (2008) 133001.
[36] J. McKenna, A.M. Sayler, B. Gaire, N.G. Johnson, M. Zohrabi, K.D. Carnes, B.D. Esry, I. Ben-Itzhak, J. Phys. B: At. Mol. Opt. Phys. 42 (2009) 121003.
[37] I. Ben-Itzhak, et al., Phys. Rev. A 78 (2008) 063419.
[38] J.D. Alexander, et al., J. Phys. B: At. Mol. Opt. Phys. 42 (2009) 154027.
[39] A. Kiess, D. Pavičić, T.W. Hänsch, H. Figger, Phys. Rev. A 77 (2008) 053401.
[40] A. Rudenko, B. Feuerstein, K. Zrost, V.L.B. de Jesus, Th. Ergler, C. Dimopoulou, C.D. Schröter, R. Moshammer, J. Ullrich, J. Phys. B. 38 (2005) 487.
[41] S. Saugout, C. Cornaggia, Phys. Rev. A 73 (2006) 041406.
[42] I.A. Bocharova, H. Mashiko, M. Magrakvelidze, D. Ray, P. Ranitovic, C.L. Cocke, I.V. Litvinyuk, Phys. Rev. A 77 (2008) 053407.
[43] J.H. Shirley, Phys. Rev. 138 (1965) B979.
[44] A.D. Bandrauk, M.L. Sink, J. Chem. Phys. 74 (1981) 1110.
[45] J.H. Posthumus, J.F. McCann, Molecules and Clusters in Intense Laser Fields, Cambridge University Press, 2001.
[46] P.H. Bucksbaum, A. Zavriyev, H.G. Muller, D. Schumacher, Phys. Rev. Lett. 42 (1990) 1883.
[47] D.S. Murphy, et al., J. Phys. B. 40 (2007) S359.
[48] K. Codling, L.J. Frasinski, P.A. Hatherly, J. Phys. B 21 (1988) L433.
[49] M.F. Kling, Ch. Siedschlag, A.J. Verhoef, J.I. Khan, M. Schultze, Th. Uphues, Y. Ni, M. Uiberacker, M. Drescher, F. Krausz, M.J.J. Vrakking, Science 312 (2006) 246.
[50] M.F. Kling, Ch. Siedschlag, I. Znakovskaya, A.J. Verhoef, S. Zherebtsov, F. Krausz, M. Lezius, M.J.J. Vrakking, Molecular Phys. 106 (2) (2008) 455.
[51] P.B. Corkum, Phys. Rev. Lett. 71 (1993) 1994.
[52] H. Niikura, F. Légare, R. Hasbani, A.D. Bandrauk, M.Y. Ivanov, D.M. Villeneuve, P.B. Corkum, Nature 417 (2002) 917.
[53] H. Niikura, F. Légare, R. Hasbani, M.Y. Ivanov, D.M. Villeneuve, P.B. Corkum, Nature 421 (2003) 826.
[54] S. Baier, C. Ruiz, L. Plaja, A. Becker, Phys. Rev. A 74 (2006) 033405.
[55] S. Baker, J.S. Robinson, C.A. Haworth, H. Teng, R.A. Smith, C.C. Chirila, M. Lein, J.W.G. Tisch, J.P. Marangos, Science 312 (2006) 424.
[56] L.J. Frasinski, J. Plumridge, J.H. Posthumus, K. Codling, P.F. Taday, E.J. Divall, A.J. Langley, Phys. Rev. Lett. 86 (2000) 2541.
[57] C. Trump, H. Rottke, W. Sandner, Phys. Rev. A. 59 (1999) 2858.
[58] Th. Ergler, A. Rudenko, B. Feuerstein, K. Zrost, C.D. Schröter, R. Moshammer, J. Ullrich, J. Phys. B 39 (2006) S493.
[59] C.R. Calvert, et al., J. Phys.: Conf. Ser. 58 (2007) 379.
[60] A.S. Alnaser, et al., Phys. Rev. A 72 (2005) 030702.
[61] A.S. Alnaser, et al., J. Phys. B. 39 (2006) S485.
[62] R.W. Robinett, Phys. Rep. 392 (2004) 1.
[63] X. Urbain, B. Fabre, E.M. Staicu-Casagrande, N. de Ruette, V.M. Andrianarijaona, J. Jureta, J.H. Posthumus, A. Saenz, E. Baldit, C. Cornaggia, Phys. Rev. Lett. 92 (2004) 163004.
[64] A. Saenz, J. Phys. B: At. Mol. Opt. Phys. 33 (2000) 4365.
[65] T.K. Kjeldsen, L.B. Madsen, Phys. Rev. Lett. 95 (2005) 073004.
[66] C.R. Calvert, T. Birkeland, R.B. King, I.D. Williams, J.F. McCann, J. Phys. B: At. Mol. Opt. Phys. 41 (2008) 205504.
[67] J. McKenna, et al., J. Mod. Opt. 54 (2007) 1127.
[68] D.S. Murphy, C.R. Calvert, J. McKenna, I.D. Williams, J.F. McCann, J. Phys.: Conf. Ser. 58 (2007) 371.
[69] H. Niikura, D.M. Villeneuve, P.B. Corkum, Phys. Rev. A. 73 (2006) 021402.
[70] Th. Ergler, A. Rudenko, B. Feuerstein, K. Zrost, C.D. Schröter, R. Moshammer, J. Ullrich, Phys. Rev. Lett. 97 (2006) 193001.
[71] A. Rudenko, Th. Ergler, B. Feuerstein, K. Zrost, C.D. Schröter, R. Moshammer, J. Ullrich, Chem. Phys. 329 (2006) 193.
[72] F. Légare, K.F. Lee, A.D. Bandrauk, D.M. Villeneuve, P.B. Corkum, J. Phys. B. 39 (2006) S503.
[73] T.E. Sharp, Atomic Data 2 (1971) 119.
[74] B. Feuerstein, U. Thumm, Phys. Rev. A 67 (2003) 063408.
[75] U. Thumm, T. Niederhausen, B. Feuerstein, Phys. Rev. A 77 (2008) 063401.
[76] B. Feuerstein, Th. Ergler, A. Rudenko, K. Zrost, C.D. Schröter, R. Moshammer, J. Ullrich, T. Niederhausen, U. Thumm, Phys. Rev. Lett. 99 (2007) 153002.
[77] V. Roudnev, B.D. Esry, Phys. Rev. A 76 (2007) 023403.
[78] M.R. Hermann, J.A. Fleck, Phys. Rev. A 38 (1988) 6000.
[79] D.S. Murphy, J. McKenna, C.R. Calvert, I.D. Williams, J.F. McCann, New J. Phys. 9 (2007) 260.
[80] D.R. Bates, J. Chem. Phys. 19 (1951) 1122.
[81] J.T. Lin, T.F. Jiang, Phys. Rev. A 63 (2000) 013408.
[82] C.R. Calvert, et al., J. Modern Opt. 56 (9) (2009) 1060.
[83] T. Niederhausen, U. Thumm, Phys. Rev. A 77 (2008) 013407.
[84] H. Niikura, D.M. Villeneuve, P.B. Corkum, Phys. Rev. Lett. 92 (2004) 133002.
[85] M. Awasthi, A. Saenz, J. Phys. B. 39 (2006) S389.
[86] H.A. Leth, L.B. Madsen, J.F. McCann, Phys. Rev. A 76 (2007) 033414.
[87] S. Selstø, M. Førre, J.P. Hansen, L.B. Madsen, Phys. Rev. Lett. 95 (9) (2005) 093002.
[88] T.K. Kjeldsen, L.B. Madsen, J.P Hansen, Phys. Rev. A 74 (2006) 035402.

[89] C.D. Lin, X.M. Tong, T. Morishita, J. Phys. B 39 (2006) S419.
[90] M. Magrakvelidze, H. Feng, T. Niederhausen, I.V. Litvinyuk, U. Thumm, Phys. Rev. A. 79 (3) (2009) 033410.
[91] H. Stapelfeldt, T. Seideman, Rev. Modern Phys. 75 (2) (2003) 543.
[92] R. Torres, R. de Nalda, J.P. Marangos, Phys. Rev. A 72 (2005) 023420.
[93] C.B. Madsen, L.B. Madsen, S.S. Viftrup, M.P. Johansson, T.B. Poulsen, L. Holmegaard, V. Kumarappan, K.A. Jørgensen, H. Stapelfeldt, Phys. Rev. Lett. 102 (2009) 073007.
[94] S. Fleischer, I.S. Averbukh, Y. Prior, Phys. Rev. A 74 (2006) 041403.
[95] O. Ghafur, A. Rouzée, A. Gijsbertsen, W.K. Siu, S. Stolte, M.J.J. Vrakking, Nature Phys. 5 (2009) 289.
[96] E. Hertz, O. Faucher, B. Lavorel, F. Dalla Via, R. Chaux, Phys. Rev. A 61 (2000) 033816.
[97] P.W. Dooley, I.V. Litvinyuk, K.F. Lee, D.M. Rayner, M. Spanner, D.M. Villeneuve, P.B. Corkum, Phys. Rev. A 68 (2003) 023406.
[98] K.P. Huber, G. Herzberg, Molecular Spectra and Molecular Structure IV. Constants of Diatomic Molecules, Van Nostrand: Reinhold, New York, 1979.
[99] Th. Ergler, A. Rudenko, B. Feuerstein, K. Zrost, C.D. Schröter, R. Moshammer, J. Ullrich, Phys. Rev. Lett. 97 (2006) 103004.
[100] E. Goll, G. Wunner, A. Saenz, Phys. Rev. Lett. 97 (2006) 103003.
[101] H. Bredhol, G. Herzberg, Can. J. Phys. 51 (1973) 867.
[102] L. Fang, G.N. Gibson, Phys. Rev. Lett. 100 (2008) 103003.
[103] X.M. Tong, C.D. Lin, Mod. Phys. Lett. B 18 (2004) 1659.
[104] S. Baker, et al., Phys. Rev. Lett. 101 (2008) 053901.
[105] M. Lein, J. Phys. B: At. Mol. Opt. Phys. 40 (2007) R135.
[106] J. Itatani, et al., Nature 432 (2004) 867.
[107] H. Stapelfeldt, Nature 432 (2004) 809.
[108] M.Y. Emelin, M.Y. Ryabikin, A.M. Sergeev, New. J. Phys. 10 (2008) 025026.
[109] M. Shapiro, P. Brumer, Principles of the Quantum Control of Molecular Processes, John Wiley & Sons, Hoboken, New Jersey, 2003; M. Shapiro, P. Brumer, Rep. Prog. Phys. 66 (6) (2003) 859.
[110] S.A. Rice, M. Zhao, Optical Control of Molecular Dynamics, Wiley, New York, 2000.
[111] I.A. Walmsley, H. Rabitz, Phys. Today 56 (2003) 43–49.
[112] H. Niikura, P.B. Corkum, D.M. Villeneuve, Phys. Rev. Lett. 90 (2003) 203601.
[113] R.B. King, et al. Central Laser Facility (UK) Annual Report, (2007–2008) pp. 82–84.
[114] X.M. Tong, C.D. Lin, Phys. Rev. Lett. 98 (2007) 123002.
[115] F. He, A. Becker, J. Phys. B 41 (2008) 074017.
[116] V. Roudnev, B.D. Esry, Phys. Rev. Lett. 99 (2007) 220406.
[117] D. Geppert, P. von den Hoff, R. de Vivie-Riedle, J. Phys. B 41 (2008) 074006.
[118] T. Brixner, G. Gerber, Chem. Phys. Chem. 4 (2003) 418.
[119] V.V. Lozovoy, X. Zhu, T.C. Gunaratne, D.A. Harris, J.C. Shane, M. Dantus, J. Phys. Chem. A 112 (17) (2008) 3789–3812.
[120] T. Laarmann, I. Shchatsinin, P. Singh, N. Zhavoronkov, C.P. Schulz, I.V. Hertel, J. Phys. B. At. Mol. Opt. Phys. 41 (2008) 074005.
[121] F. Remacle, R.D. Levine, PNAS 103 (2006) 6792.
[122] R.E. Carley, E. Heesel, H.H. Fielding, Chem. Soc. Rev. 11 (2005) 949.
[123] M. Fushitani, Annu. Rep. Prog. Chem., Sect. C 104 (2008) 272.
[124] http://flash.desy.de/.
[125] http://ssrl.slac.stanford.edu/lcls/.
[126] E. Goulielmakis, et al., Science 320 (2008) 1614.
[127] F. Krausz, M. Ivanov, Rev. Modern Phys. 81 (2009) 163–234.
[128] P.B. Corkum, F. Krausz, Nature Phys. 3 (6) (2007) 381–387.
[129] M. Nisoli, G. Sansone, Prog. Quantum Electron. 33 (1) (2009) 17–59.
[130] F. Kelkensberg, et al., Phys. Rev. Lett. 103 (2009) 123005.
[131] A.T.J.B. Eppink, D.H. Parker, Rev. Sci. Instr. 68 (1997) 3477.
[132] H.A. Leth, L.B. Madsen, K. Mølmer, Phys. Rev. Lett. 103 (2009) 183601.
[133] M. Kramer, et al., Phys. Rev. Lett. 103 (2009) 213003.
[134] C.R. Calvert, R.B. King, W.A. Bryan, W.R. Newell, J.F. McCann, J.B. Greenwood, I.D. Williams, J. Phys. B. 43 (2010) 011001.